

Evidence of kilometer-wide shallow bulk plastic yielding along the 2021 Maduo, Tibet, surface rupture, and its relation with the dynamic rupture process

Solene L Antoine¹, Zhen Liu², Arthur Delorme³, and Yann Klinger⁴

¹Jet Propulsion Laboratory, California Institute of Technology, Pasadena, CA, USA

²California Institute of Technology

³Institut De Physique Du Globe De Paris

⁴Université de Paris Cité, Institut de physique du globe de Paris, CNRS

January 21, 2024

Abstract

Surface deformation associated with continental earthquake ruptures includes localized deformation on the faults, as well as deformation in the surrounding medium through distributed and/or diffuse processes. However, the connection of the diffuse part of the surface deformation to the overall rupture process, as well as its underlying physical mechanisms are not yet well understood. Computing high-resolution optical image correlations for the 2021/05/21 Mw7.4 Maduo, Tibet, rupture, we highlight a correlation between the presence of faults and fractures at the surface, and variations in the across-fault displacement gradient, fault zone width, and amplitude of surface displacement. We show that surface slip along primary faults is systematically associated with gradients greater than 1%, and is dominant in regions of greater coseismic surface displacement. Conversely, the diffuse deformation is associated with gradients $\approx 0.3\%$, and is dominant in regions of lesser surface displacement. The distributed deformation then occurs for intermediate gradients of 0.3-1%, and at the transition between the localized and diffuse deformation regions. Such patterns of deformation are also described in laboratory experiments of rock deformation, themselves supported by field observations. Comparing these experiments to our observations, we demonstrate that the diffuse deformation along the 2021 Maduo rupture corresponds to kilometer-wide plastic yielding of the bulk medium occurring in regions where surface rupture is generally missing. Along the 2021 Maduo rupture, diffuse deformation occurs primarily in the epicentral region, where the dynamic stresses associated with the nascent pulse-like rupture could not overcome the shallow fault zone frictional strength.

1 **Evidence of kilometer-wide shallow bulk plastic yielding along the 2021 Maduo, Tibet,**
2 **surface rupture, and its relation with the dynamic rupture process**

3

4 S. L. Antoine^{1,2}, Z. Liu¹, A. Delorme², Y. Klinger²

5 ¹ NASA Jet Propulsion Laboratory, California Institute of Technology, Pasadena, California,
6 USA

7 ² Université de Paris Cité, Institut de physique du globe de Paris, CNRS, Paris, France,

8

9 Corresponding author: Solène L. Antoine (solene.antoine@jpl.nasa.gov)

10

11 **Key points:**

- 12 - The 2021 Maduo earthquake is dominantly associated with kilometer-scale surface
13 diffuse bulk plastic yielding.
- 14 - Diffuse bulk plastic yielding occurs in regions where the dynamic stresses could not
15 overcome the shallow fault zone frictional strength.
- 16 - This study documents a gradual surface deformation localization along the rupture strike
17 as a function of coseismic displacement.

18

19 **Abstract**

20 Surface deformation associated with continental earthquake ruptures includes localized
21 deformation on the faults, as well as deformation in the surrounding medium though distributed
22 and/or diffuse processes. However, the connection of the diffuse part of the surface deformation
23 to the overall rupture process, as well as its underlying physical mechanisms are not yet well

24 understood. Computing high-resolution optical image correlations for the 2021/05/21 M_w 7.4
25 Maduo, Tibet, rupture, we highlight a correlation between the presence of faults and fractures at
26 the surface, and variations in the across-fault displacement gradient, fault zone width, and
27 amplitude of surface displacement. We show that surface slip along primary faults is
28 systematically associated with gradients greater than 1%, and is dominant in regions of greater
29 coseismic surface displacement. Conversely, the diffuse deformation is associated with gradients
30 $\leq 0.3\%$, and is dominant in regions of lesser surface displacement. The distributed deformation
31 then occurs for intermediate gradients of 0.3-1%, and at the transition between the localized and
32 diffuse deformation regions. Such patterns of deformation are also described in laboratory
33 experiments of rock deformation, themselves supported by field observations. Comparing these
34 experiments to our observations, we demonstrate that the diffuse deformation along the 2021
35 Maduo rupture corresponds to kilometer-wide plastic yielding of the bulk medium occurring in
36 regions where surface rupture is generally missing. Along the 2021 Maduo rupture, diffuse
37 deformation occurs primarily in the epicentral region, where the dynamic stresses associated
38 with the nascent pulse-like rupture could not overcome the shallow fault zone frictional strength.

39

40 **Plain Language**

41 Surface deformation associated with major continental earthquakes generally occurs along faults
42 which are visible at the surface. However, in the case of the 2021 M_w 7.4 Maduo, Tibet, rupture,
43 the surface rupture exhibits a discounted trace with kilometer-long gaps, and a primarily diffuse
44 surface deformation, raising the following question: What processes can explain the primarily
45 diffuse deformation along the 2021 Maduo surface rupture? Calculating high-resolution (0.5 m)
46 displacement maps along the 2021 Maduo rupture area, we highlight that the diffuse deformation

47 gradients, which can have a kilometer-wide extension across the fault zone, accommodate up to
48 1.5 m of ground surface displacement in regions where the faults did not rupture. Deriving
49 evolution laws for the different deformation components, we highlight a gradual increase of the
50 displacement localization along the faults with increasing total surface displacement. We then
51 suggest that the diffuse deformation corresponds to diffuse plastic deformation of the rock
52 medium in regions of lesser earthquake displacement, where the faults could not rupture totally
53 throughout the surface. Such diffuse behavior is found primarily in the epicentral area, where the
54 earthquake displacement and associated stresses are lower due to the smaller size of the nascent
55 rupture patch.

56

57 **Keywords**

58 High-resolution optical image correlation, Maduo, surface displacement, localized, diffuse,
59 distributed deformation, frictional strength, dynamic rupture process

60

61 **1. Introduction**

62 Fault zones are usually described as confined and layered structures composed of series of
63 primary faults where the majority of the co-seismic deformation occurs, and surrounded by a
64 fractured medium also referred to as the damage zone hosting distributed deformation (Mitchell
65 and Faulkner, 2009; Torabi et al., 2019). However, geodetic (Antoine et al., 2021, 2022; Fialko
66 et al., 2005; Hearn and Fialko, 2009; C. Li et al., 2022; Materna and Bürgmann, 2016), field
67 (Petersen et al., 2011; Rodriguez Padilla and Oskin, 2023), and seismic observations (e.g.,
68 Alongi et al., 2022; Perrin et al., 2021; Qiu et al., 2021; Vidale and Li, 2003; Yang, 2015; Yang
69 et al., 2011; Zhou et al., 2022) also showed the existence of a third deformation region, at the

70 transition between the damage zone and the surrounding intact medium, where diffuse plastic
71 yielding of the rocks would occur. This deformation region is referred to as the diffuse
72 deformation zone (Antoine et al., 2021, 2022). Consequently, the total earthquake surface
73 deformation expresses as a combination of localized deformation on the primary faults,
74 distributed deformation on the secondary fractures, and diffuse deformation in the surrounding
75 medium. Each of these deformation components occurs at a different spatial scale, and together
76 they outline the area where the inelastic permanent deformation takes place (e.g., Barnhart et al.,
77 2020; Rodriguez Padilla et al., 2022; Scott et al., 2018) which we refer to as the Fault Zone (FZ)
78 in this study.

79

80 On one hand, the localized deformation corresponds to the surface slip that occurs on the well-
81 defined faults, and usually affects a region of a few meters to a few tens of meters wide. Such
82 localized deformation has been characterized along numerous surface ruptures by mapping the
83 faults, and measuring displacement offsets across anthropic and geomorphic features (e.g.,
84 Klinger et al., 2005; Rockwell et al., 2002; Teran, 2015). On the other hand, the distributed and
85 diffuse components of the deformation, together, constitute what is called the off-fault
86 deformation (OFD). OFD affects regions hundreds of meters to a few kilometers away from the
87 primary faults (e.g., Antoine et al., 2021, 2022; Milliner et al., 2016; Mitchell and Faulkner,
88 2009; Rodriguez Padilla et al., 2022). Within the OFD, the distributed deformation, as defined in
89 this study, corresponds to deformation occurring on series of secondary fractures located away
90 from the main rupture (see also Nurminen et al., 2022; Simone et al., 2022). Because the
91 fractures are visible at the surface, the distributed deformation can be detected in the field or
92 using optical and/or topography data (e.g., Choi et al., 2018; Gold et al., 2015; Simone et al.,

93 2022). The diffuse deformation, however, is not directly associated with visible fractures and
94 generates continuous kilometer-scale gradients of ground surface displacement which can only
95 be detected using dense geodetic measurements with wide across-fault apertures (Antoine et al.,
96 2021; Antoine et al., 2022; Fialko et al., 2005; Li et al., 2022). Consequently, diffuse
97 deformation is often not reported and included in earthquake displacement budgets, and its role
98 in the rupture process is ignored.

99

100 As an inelastic process, though, the diffuse deformation should also affect the mechanical
101 properties of the crustal medium as it is described for the more densely fractured damage zone
102 (Budiansky and O'connell, 1976; Heap et al., 2010; Laws et al., 2003; Yamamoto et al., 2002).
103 Accumulation of such wide inelastic deformation over time would then lead to a compliant
104 behavior of the FZ at wider scale than usually considered (Fialko et al., 2002; Hearn and Fialko,
105 2009; Materna and Bürgmann, 2016; Rodriguez Padilla and Oskin, 2023). These modifications
106 in the FZ mechanical behavior have an impact on the rupture process, at the scale of an
107 individual earthquake rupture (Barbot et al., 2008; Gombert et al., 2018; Okubo, 2019; Sammis
108 et al., 2009; Zhao et al., 2023), as well over several seismic cycles (Faulkner et al., 2006;
109 Lyakhovsky and Ben-Zion, 2008; Passelègue et al., 2018). Hence, it is critical to improve the
110 characterization of the diffuse deformation, and understand the underlying physical processes
111 and its role in the rupture process and FZ development.

112

113 Here, we use high-resolution optical image correlation (OIC) to measure the surface horizontal
114 displacement field associated with the 2021 Maduo earthquake rupture. Horizontal displacement
115 maps allow analyzing the along-strike evolution of the surface displacement and deformation

116 patterns, including the contribution of each deformation component along with the total surface
117 displacement, the width of the deformation zone (also called fault zone width, FZW), and the
118 tectonic and co-seismic rupture settings. Comparing the OIC measurements with published
119 observations from field and laboratory experiments, this study first aims at demonstrating the
120 permanent and inelastic nature of the diffuse deformation, and then proposing plausible physical
121 underlying mechanisms.

122

123 **2. The 2021 M_w 7.4 Maduo, Tibet, rupture**

124 The 2021 Maduo earthquake rupture occurred along the left-lateral strike-slip Jiangcuo fault,
125 within the Bayan Har block of the Eastern Tibetan plateau, at about 100 km South of the Kunlun
126 fault (Ha et al., 2022; Ren et al., 2022). The geometry and slip rate of the Jiangcuo fault are
127 poorly known. However, paleoseismic studies suggest a slip rate of 0.35-0.55 mm/yr (Pan et al.,
128 2022; Ren et al., 2022). Analysis of geomorphic offsets showed a possible cumulative fault
129 displacement of ~4-5 km, decreasing towards the SE side of the fault (Li et al., 2022). On May
130 21, 2021 a rupture nucleated at a depth of ~10-17 km, and propagated bilaterally for a total
131 rupture length of ~160 km (Fan et al., 2022; He et al., 2021; Liu et al., 2022; Wei et al., 2022).
132 Published earthquake rupture models suggest a maximum slip of ~5-6 m located at ~3-5 km
133 depth, dominated by mostly left-lateral displacement (e.g., He et al., 2021; Jin and Fialko, 2021;
134 Wei et al., 2022; Xiong et al., 2022). Despite its magnitude, the localized surface rupture
135 associated with the 2021 Maduo event is very discontinuous, and surface deformation occurred
136 for a large part on distributed fractures (Liu et al., 2023; Pan et al., 2022; Ren et al., 2022, 2021;
137 Xie et al., 2022; Yuan et al., 2022). Continuous surface ruptures are primarily reported along the
138 NW and SE extremities of the rupture, while they are separated by two major rupture gaps in the

139 central part. Field studies reported both left-lateral and vertical offsets with respective maximum
140 amplitudes of 2.6-2.9 m and 0.95-1.8 m (Pan et al., 2022; Ren et al., 2022, 2021; Xie et al., 2022;
141 Yuan et al., 2022). The horizontal component, however, is dominant in the surface deformation,
142 and most horizontal offsets range between 0.5-1.5 m. On average, along the 160-km rupture, the
143 average left-lateral surface displacement from field observations is 0.4 m (Yuan et al., 2022),
144 whereas geodetic studies report average values of ~2-3 m (Jin and Fialko, 2021; Li et al., 2022).
145 This difference is interpreted as a result of large OFD along the Maduo rupture (Li et al., 2022),
146 which corresponds to the distributed and diffuse deformations occurring off the primary faults.
147 Overall, the Maduo earthquake presents an heterogeneous surface deformation, with along-strike
148 transitions from regions where localized deformation is dominant, located along mapped faults,
149 to regions where OFD is dominant. In this regard, the 2021 Maduo rupture constitutes a unique
150 case example for analyzing the patterns of localized, the distributed, and the diffuse
151 deformations, their spatial interactions, as well as the underlying physical mechanisms.

152

153 **3. Material and Methods**

154 We use high-resolution OIC to capture the near-fault surface displacement associated with the
155 2021 Maduo rupture. Data include high-resolution stereo and tri-stereo pre-earthquake SPOT6-7
156 (1.6 m ground sampling distance, gsd) and post-earthquake Pleiades (0.5 m gsd) satellite optical
157 images. In total, fourteen combinations of pre- and post-earthquake images were used to cover
158 the 160 km-long study area from East to West (Fig. S1). All data are downloaded on a High-
159 Performance Computer, and processed using the MicMac correlation photogrammetry and OIC
160 software (Rosu et al., 2015; Rupnik et al., 2017), along with Python, MATLAB, and GDAL for
161 the pre- and post-processing. Pleiades data cover only a ± 5 km-wide swath along the 2021

162 Maduo rupture trace (Figs. 1a,b and S1) thus the calculations are performed only within this area.
163 Even though SPOT6/7 pre-earthquake images have a 1.6 m gsd, all processing steps are
164 performed at a 0.5 m gsd which is the native gsd of the Pleiades images. Impact of the
165 resampling and choice of the common gsd (between 0.5 and 1.6 m) have been tested, and the 0.5
166 m-gsd results are showing smaller variability and average noise level (Fig. S2).

167
168 For each sub-area of the rupture, covered by different high-resolution image pools, (tri-)stereo
169 images from both the pre- and post-earthquake periods are used to calculate, respectively, pre-
170 and post-earthquake Digital Surface Models (DSM). The DSMs are used to orthorectify
171 (correction from viewing angle and topography distortions, and projection in a common ground
172 reference; Leprince et al., 2007; Rupnik et al., 2016) the pre- and post-earthquake optical images,
173 respectively. By using DSMs directly computed from the same images later used for OIC, one
174 reduces possible orthorectification bias due to the use of low-resolution topography models, and
175 georeferencing errors. In addition, the use of distinct pre- and post-earthquake DSMs to
176 orthorectify images acquired before and after the earthquake allows avoiding any error related to
177 change in the topography due to the earthquake. Pairs of pre- and post-earthquake orthorectified
178 images are then cropped to their common areas to perform the OIC. OIC is performed using a
179 correlation window of 2.5 m (5 pixels), a search window of 5-7 m, a sub-pixel correlation step of
180 $1/20^{\text{th}}$ of pixel, and a regularization term of 0.3. Taking advantage of the fact that we could use
181 two to three images both for the pre- and post-earthquake periods, we performed OIC for all the
182 possible pairs straddling the earthquake date, and stacked the best results. Stacking operation is
183 performed using a weighted average method based on the correlation score maps output of the
184 OIC process (Delorme et al., 2020). Each pixel is weighted using its correlation score (0-1),

185 allowing for an increase of the signal to noise ratio. The final stacked OIC results obtained for
186 different sub-areas are corrected for ramp artifacts (bundle block adjustment residual) using
187 lower-resolution SAR-derived horizontal displacement maps from Liu et al. (2022) that provide
188 a common reference. A polynomial function is modeled to the difference between SAR and OIC
189 at low frequency, and removed from the OIC results (Fig. S3a-e). Sentinel-2B OIC was also
190 performed to cross-check the quality of the ramp corrections, and validate our method of ramp
191 removal using SAR results (Figs. S3f and S4). Overall, this method preserves the high-frequency
192 signal, that corresponds to the FZ deformation, along with some other local artefacts
193 (decorrelation in regions with clouds, or affected by large sedimentary transport such as
194 drainages, wetlands and dune fields; Fig. 1a). Through specific shape and/or direct visual
195 identification on optical images, we identified local artefacts and ignored them when performing
196 the analysis of the earthquake-related displacements.

197

198 Finally, we tested the possibility of measuring the vertical displacements from the difference in
199 elevation between the post-earthquake and the pre-earthquake DSMs, whose features have been
200 horizontally realigned using the measured horizontal displacement (Antoine et al., 2021, 2022;
201 Delorme et al., 2020). However, except for one area (Fig. S5), the noise level reaches an
202 amplitude ± 1 m, which prevents any systematic analysis of the vertical deformation. Thus, from
203 here, our work focuses only on the horizontal components of the surface displacement.

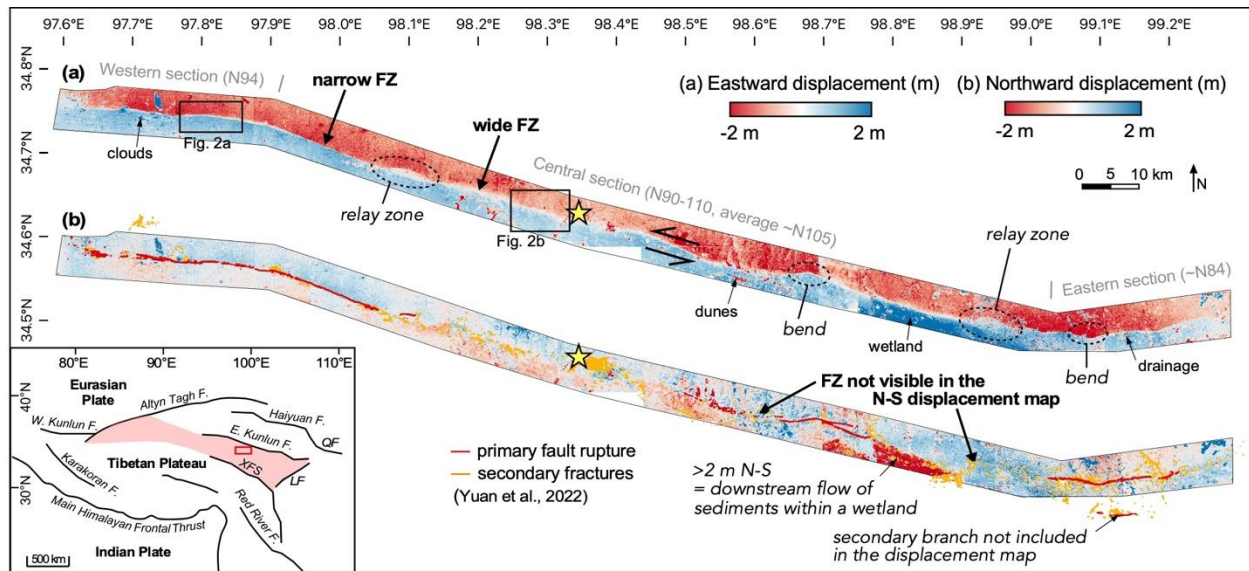
204

205 **4. Results**

206 **4.1. Horizontal surface displacement maps**

207 Horizontal surface displacement measured from OIC along the 2021 Maduo earthquake show
208 dominant East-West component, with relative amplitude reaching ± 2 m (Fig. 1a), while the
209 North-South component, when excluding the high-displacement geomorphic artefacts, is limited
210 to ± 1 m and is only detectable in a few places (Fig. 1b). This is consistent with the left-lateral
211 strike-slip motion determined from seismological and geodetic data (Fan et al., 2022; K. He et
212 al., 2021; Q. Li et al., 2022; Wang et al., 2021; Wei et al., 2022; Zhang et al., 2022; Jin and
213 Fialko, 2021; C. Li et al., 2022; Li et al., 2023; Liu et al., 2022; Xiong et al., 2022; Xu et al.,
214 2021, 2021; Yang et al., 2022; Zhao et al., 2021), and from field observation (Pan et al., 2022;
215 Ren et al., 2022, 2021; Xie et al., 2022; Yuan et al., 2022). The area affected by surface
216 deformation during the 2021 Maduo event, referred to as the FZ, is clearly visible in the OIC
217 results, and its geometry is consistent with the field rupture mapping (Fig. 1b). The FZW
218 corresponds to the width of the area showing a gradient of displacement between the two sides of
219 the fault, as seen on the across-fault displacement profiles (Fig. 2). FZW varies significantly
220 along the rupture, including narrow FZs that correlate with the localized ground ruptures (red
221 lines, Fig. 1b), and wide FZs, from few hundreds of meters to kilometers, that correspond to
222 regions of distributed fracturing (orange lines, Fig. 1b) or rupture gaps (no visible ground
223 ruptures, Fig. 1b). Rupture azimuth variations associated with local geometrical asperities are
224 also found all along the Maduo FZ, with three main distinct sections that are separated by two
225 major fault bends, respectively located at longitude 97.9°E and 99.0°E . The central section
226 strikes WNW-ESE ($\sim\text{N}105$), whereas the Eastern and Western sections strike E-W ($\sim\text{N}84$ and
227 $\sim\text{N}94$, respectively).

228



229

230 **Figure 1: (a) East-West and (b) North-South surface displacement along the 2021 Maduo**

231 **rupture measured at 0.5 m gsd from the correlation of pre-earthquake SPOT6/7 images**

232 **and post-earthquake Pleiades images (see methodology for gsd details). The Fault Zone**

233 **(FZ) appears as a continuous and curvilinear structure separating the NE and the SW**

234 **blocks. Some geometrical complexities, including bends and relay zones, are indicated**

235 **using dashed-line circles. Examples of artefacts related to geomorphic or meteorologic**

236 **processes are indicated using thin black arrows. Epicenter location, from global CMT**

237 **catalog (GCMT), is shown with a yellow star. Field rupture map from Yuan et al., 2022 is**

238 **overlaid in (b) with, in red, the primary ruptures, and in orange, the secondary fractures.**

239 **Inset at the bottom left shows the tectonic context, modified from Ren et al. (2022). Light**

240 **red area is the Bayan Har block. Red box is the area of (a). LF is the Longmenshan Fault.**

241 **XFS is the Xianshuihe Fault System. QF is the Qinling Fault.**

242

243 **4.2. Separating the localized, distributed and diffuse components of the deformation**

244 We use stacked profiles to analyze how the fault-parallel surface displacement distributes
245 between the localized deformation on faults, the distributed deformation on fractures, and the
246 diffuse deformation. Stack boxes are 200-m wide, and displacement results are stacked within
247 the boxes using a weighted median method that uses the output OIC correlation score. Fault-
248 parallel displacement is derived from the combination of the East-West and North-South
249 displacement along the stack profile with respect to the local fault azimuth (StackProf software).

250

251 **4.2.1. Individual profile analysis**

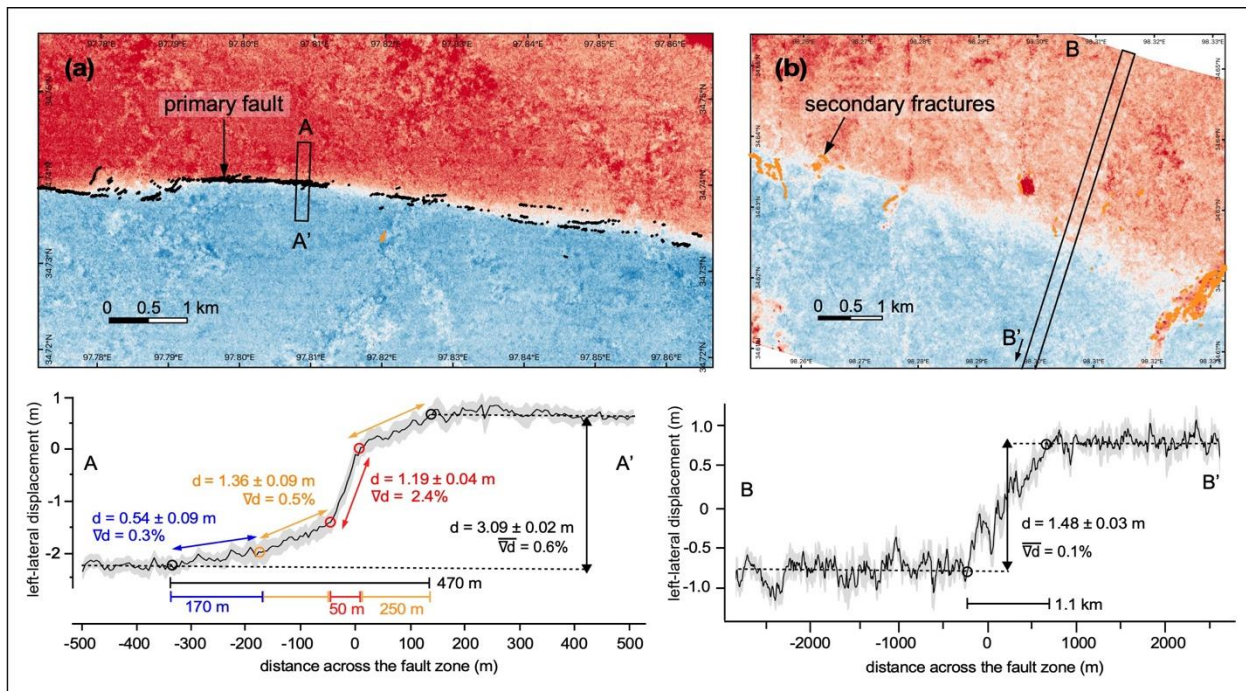
252 Individual profile analysis is performed following the method of Antoine et al. (2021, 2022) to
253 measure the localized, distributed and diffuse components of the deformation. Similar methods
254 are widely used to characterize earthquake surface deformation based on OIC results, though
255 profile widths and lengths can vary (Ayorlou et al., 2021; Barnhart et al., 2020; Delorme et al.,
256 2020; Gold et al., 2015; Li et al., 2022; Milliner et al., 2016; Scott et al., 2018). In this study,
257 similar to Antoine et al. (2021, 2022), the length of profiles ranges from 1 (Fig. 2a) to 5 (Fig. 2b)
258 km, allowing to capture the horizontal trend outside of the diffuse deformation zone,
259 corresponding to the far-field elastic response of the media. Far-field elastic response is usually fit
260 by an arctangent function (Segall, 2010) though, because of the limited ± 5 km coverage of the
261 OIC results around the faults, it appears as an horizontal trend in the profiles.

262

263 We quantify the variations in the slope along the across-fault displacement profile, referred to as
264 displacement gradient, which reveal variations in the underlying mechanisms of deformation
265 across the FZ. For example, along profile AA' (Fig. 2a), highest displacement gradient of 2.4%
266 is observed in the center of the profile from -40 m to +10 m. This region correlates with the

267 location of a primary fault mapped in the field (black line, Fig. 2a), and thus corresponds to the
 268 localized surface deformation. The localized deformation area is clearly separated from the
 269 surrounding regions that exhibits a displacement gradient of 0.5%, and can correlate with
 270 distributed fractures in the field. We refer these second regions as the distributed deformation
 271 regions. A third region can also be distinguished on the northern side of the profile, from -175 to
 272 -345 m, where the displacement gradient approaches 0.3%. This region clearly does not show
 273 any apparent association with field-mapped fractures thus we classify it as diffuse deformation.
 274 Diffuse deformation is also inferred along the BB' profile, where 1.48 m of left-lateral
 275 displacement is accommodated with a uniform displacement gradient of 0.1% (-250 to +700 m,
 276 Fig. 2b), and across a region where only few sparse secondary fractures were identified in the
 277 field.

278



279

280 **Figure 2: Zoom in the East-West displacement map in (a) a region of primarily distributed**
 281 **deformation, and (b) a region of primarily diffuse deformation. Rupture map is from Yuan**

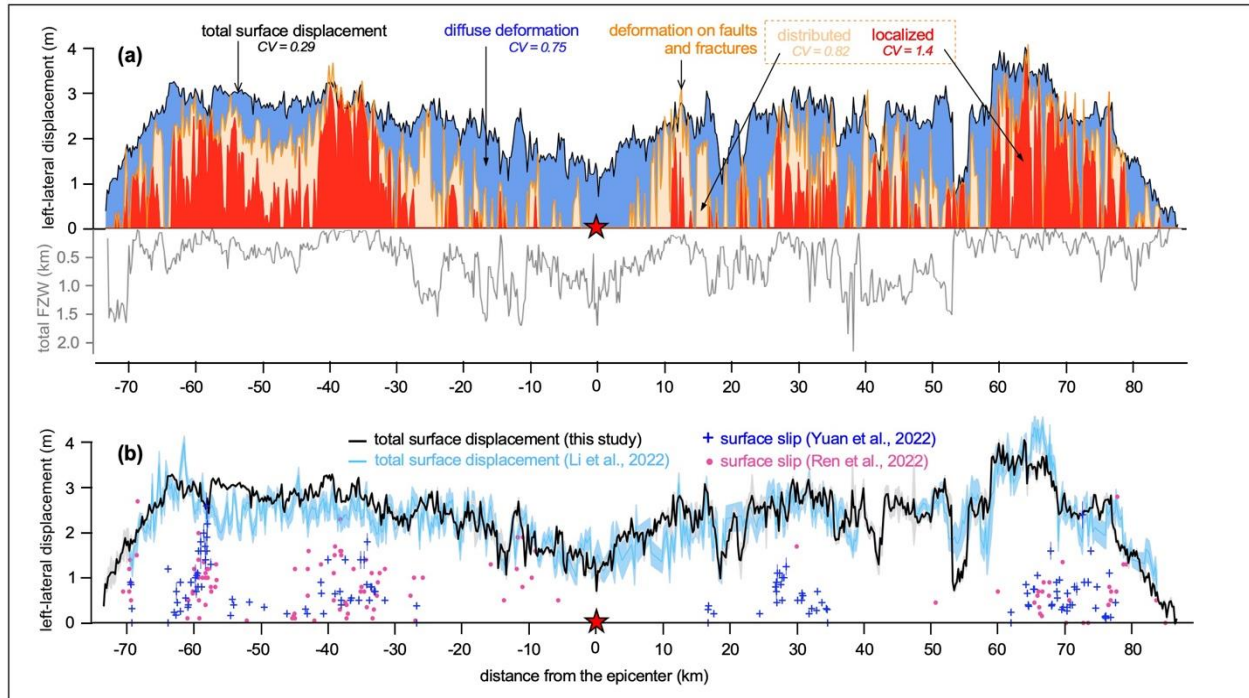
282 et al. (2022). AA' and BB' across-fault displacement profiles are presented below the
283 displacement maps. For each profile, the values of displacement d , the width over which
284 this displacement occurs (horizontal bars), and the corresponding displacement gradient
285 ∇d is indicated for the total (black), localized (red), distributed (orange) and diffuse (blue)
286 deformation regions.

287

288 4.2.2. Surface displacement budget associated with the total, localized, distributed, and 289 diffuse deformations

290 We measure the evolution of fault-parallel displacement along the rupture strike from the
291 analysis of 781 cross-fault profiles located every 200 m, together with the field rupture map from
292 Yuan et al. (2022). Using the same method as in Figure 2, within each of the 781 profiles, we
293 measure the surface displacement offset associated with the total (black curve; Fig. 3a,b),
294 localized (red area; Fig. 3a), and distributed deformations (light orange area; Fig. 3a). The
295 diffuse deformation (blue area; Fig. 3a) is then calculated from the difference between the total
296 displacement curve and the sum of the localized and distributed deformations.

297



298

299 **Figure 3: (a) Complete surface displacement budget for the 2021 Maduo rupture (top plot).**

300 **Black curve is the total surface displacement. Orange curve includes the displacement**

301 **occurring on primary faults (red area) and secondary fractures (light orange area). Diffuse**

302 **deformation corresponds to the blue area. Fault Zone Width (FZW) is shown in the bottom**

303 **plot with the grey curve. The coefficient of variation (CV) reflects the degrees of variability**

304 **of the curves, and is defined as the ratio between the standard deviation and the mean. (b)**

305 **Comparison between total displacement measured from optical OIC (curves) and faults**

306 **offsets measured in the field (points and crosses), in the left-lateral component, along the**

307 **2021 Maduo rupture. Black curve is from this study, and blue curve is from Li et al. (2022)**

308 **who used Sentinel-2B images at 10 m gsd.**

309

310 Our results first show that the total surface displacement associated with the 2021 Maduo rupture

311 ranges between 1 and 4 m (to the exception of the two rupture tips where displacement tapers to

312 zero), with the smallest displacement values reported in the epicentral region (-20 to +10 km). In
313 comparison, the largest surface displacement is measured along the eastern and western sections
314 of the rupture. On average, total surface displacement is 2.35 ± 0.09 m, and occurs over a total
315 FZW of 30 to 2215 m, which corresponds to an average total FZW of 600 m. Coefficient of
316 variation (CV) of the total displacement curve is 0.29, which is unexpectedly small considering
317 the complexity of the ruptures and the scattering of the field offsets (Fig. 3b; Pan et al., 2022;
318 Ren et al., 2022, 2021; Xie et al., 2022; Yang et al., 2022; Yuan et al., 2022). Localized
319 deformation, occurs primarily along the eastern (30 to +80 km) and western sections (-30 to -70
320 km), with no or few offsets detected along the central region of the rupture. The localized
321 deformation, on the other hand, when average along the 2021 Maduo rupture length, represents
322 0.62 ± 0.05 m, so 26.3% of the total surface displacement, and occurs over an average width of
323 87 m. The localized deformation curve represents the maximum envelop of the field data, as it is
324 usually observed for optical studies (e.g., Antoine, 2021; Milliner, 2015). The CV of the
325 localized deformation curve is 1.4, which reflects the complexity and discontinuity of the surface
326 ruptures, as evidenced in the field.

327

328 Distributed deformation is detected essentially along the eastern and western sections of the
329 Maduo rupture, and primarily alongside or at the tips of the primary fault ruptures. On average,
330 the distributed deformation is 0.67 ± 0.09 m, corresponding to 28.5% of the total surface
331 displacement budget, and occurs over an average width of 133 m around the localized
332 deformation regions. The CV of the distributed deformation curve is 0.82. Very few distributed
333 deformation is detected in the epicenter area, similar to what was observed for the localized
334 deformation. In fact, the epicenter area is mainly characterized by diffuse deformation as shown

335 by profile BB' (Fig. 2b). In contrast with the localized and distributed deformations, the diffuse
336 deformation is found along most of the rupture length (blue area, Fig. 3a). It has the largest
337 amplitudes along the epicentral area, up to ~2 m, and at the rupture tips. The average surface
338 displacement associated with the diffuse deformation component is 1.06 ± 0.09 m, representing
339 45.2% of the total surface displacement. The CV for the diffuse deformation curve is 0.75, which
340 is intermediate to that of the distributed and total displacement curves. The contrasts between
341 amplitudes and CVs of the different displacement curves thus reveal the crucial role of the
342 distributed and diffuse deformations in accommodating the total co-seismic surface displacement
343 in regions of lesser surface fault slip (Antoine et al., 2022).

344

345 **4.2.3. Evolution of the FZW**

346 The total FZW corresponds to the width of the total displacement offset, and is reported for each
347 of the 781 profiles (grey curve, Fig. 3a). For example, along the profiles AA' and BB' (Fig. 2),
348 total FZW is 480 and 1.1 km, respectively. Along the Maduo rupture, the largest FZWs, up to
349 2.15 km, are found in the epicenter area, and in part of the SE section (+35 to +53 km). Along
350 the SE section, however, the rupture propagated across swampy terrains (indicated as wetland in
351 Fig. 1) and the trace of the rupture might not have been all well preserved, leading to a possible
352 over-estimation of the total FZW. Nevertheless, the lowest FZWs are found essentially along the
353 NW and SE sections, from -65 to -30 km and +60 to +80 km. Interestingly, the epicentral area
354 also corresponds to the area of smallest surface displacement along the 2021 Maduo rupture,
355 whereas the NW and SE sections have the greatest surface displacement. Hence, we observe a
356 decrease of the FZW together with an increase of the displacement, which is in contradiction
357 with what has been previously reported in field studies (Faulkner et al., 2011; Savage and

358 Brodsky, 2011). This is likely due to that field studies most often describe only the off-fault
359 fractures affecting the first tens to hundreds of meters around the faults, which are associated
360 with dynamically activated off-fault damage that tend to increase in width with slip on the fault
361 (Faulkner et al., 2011; Okubo et al., 2019; Thomas and Bhat, 2018). Here, measurements of the
362 surface deformation are performed at a wider (>0.5 km) scale, and include the diffuse
363 deformation as part of the FZ deformation budget. The decrease of the total FZW with increasing
364 displacement thus highlights the decreasing contribution of the diffuse deformation with
365 increasing coseismic surface displacement, as inferred in previous studies (Antoine et al., 2021;
366 Perrin et al., 2016).

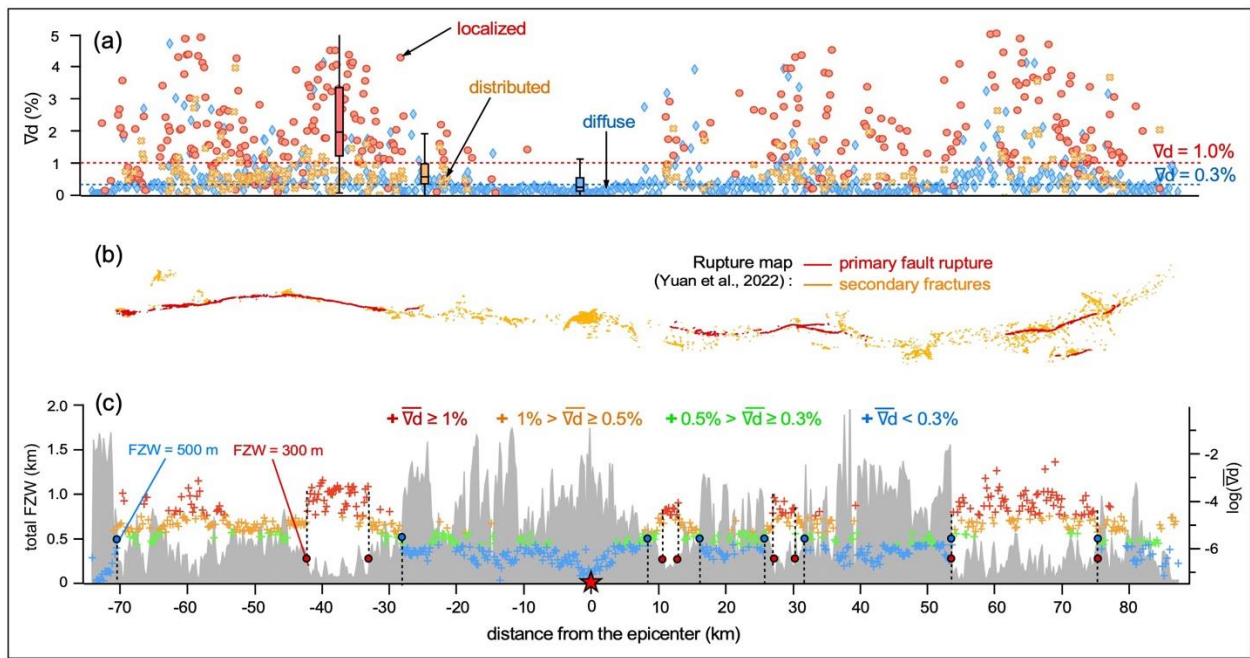
367

368 **4.3. Displacement gradient analysis**

369 **4.3.1. Localized, distributed, and diffuse displacement gradients**

370 We derive the displacement gradient ∇d , as a first order equivalent of strain, for each
371 deformation region across the FZ from the separate analysis of the displacement values and
372 widths for the localized, distributed and diffuse deformation regions. Examples are given along
373 the profiles AA' and BB' (Fig. 2), and a similar approach is applied to each of the 781 across-
374 fault profiles (Fig. 4a). Careful examination of each profile shows that the regions characterized
375 entirely by diffuse deformation, including the epicentral area, are associated with across-fault
376 displacement gradients below 0.3% (e.g., $\nabla d = 1.48/1100 = 0.0013$ in profile BB'). Statistical
377 analysis shows a median displacement gradient value of 0.2% for the diffuse deformation regions
378 with a lower (Q1) and upper (Q3) quartile values of 0.1 and 0.5%, respectively (blue barplot,
379 Fig. 4a). Distributed deformation is associated with a median displacement gradients of 0.5%,
380 and a Q1 and Q3 values of 0.3 and 1% (orange barplot, Fig. 4a). As an example, along the profile

381 AA' the distributed deformation shows a $\nabla d = 1.36/250 = 0.0054$. Finally, displacement
 382 gradients associated with the localized deformation dominantly range between 1.2% (Q1) and
 383 3% (Q3), (e.g., $\nabla d = 1.19/50 = 0.024$ in profile AA', Fig. 2a ; and red barplot in Fig. 4a). All
 384 these values are in general consistent with the results from Li et al. (2023), who detected shear
 385 strains of 0.7-5% in the regions identified as localized and/or distributed deformation. Using
 386 Sentinel-2 OIC results from Li et al. (2022), Zhao et al. (2023) also measure shear strain over the
 387 diffuse deformation regions as low as 0.1-0.2%. In the following, the lower and upper quartiles
 388 of the distributed deformation are used thresholds expressing transitions between the different
 389 deformation regimes (Fig. 4c).
 390



391
 392 **Figure 4: (a) Displacement gradients ∇d measured across the localized (red), distributed**
 393 **(orange) and diffuse (blue) deformation regions along the 2021 Maduo rupture. Barplots**
 394 **show the lower quartile (Q1), median, and upper quartile (Q3) for the ∇d measurements of**
 395 **the corresponding components. Blue and red dashed lines respectively highlight the**

396 transitions between diffuse and distributed, and distributed and localized deformation
397 regimes. (b) Field map of the 2021 Maduo surface rupture including, in red, the primary
398 faults, and in orange, the secondary fractures (Yuan et al., 2020). (c) Evolution of the total
399 FZW (grey area, Fig. 3a) and average displacement gradient across the FZ (colored
400 crosses). Color scale reflects the different ranges of displacement gradients as assessed in
401 (a). Distributed deformation is separated in two, with the value of 0.5% representing the
402 theoretical inelastic deformation threshold (Barnhart et al., 2020). Red and blue dots
403 highlight, in the FZW curve, some examples of transitions from a primarily diffuse to a
404 primarily localized surface deformation, occurring for corresponding FZW values of 300 to
405 500 m. In (a), each profile can be represented by 1 to 3 points with each point
406 corresponding to a different deformation mode, whereas in (c), each profile is represented
407 by 1 point that reflects the dominant deformation mode.

408

409 4.3.2. Average displacement gradients as a measure of the dominant mode of deformation

410 Calculating the ratio between the total displacement offset and the total FZW for each profile, we
411 analyze the evolution of the average displacement gradient $\overline{\nabla d}$ along the Maduo rupture, and
412 assess along-strike evolutions in the dominant mode of deformation (Fig. 4c). As an example, in
413 the case of profile AA' (Fig. 2a), the dominant mode of deformation is the distributed
414 deformation (accounting for 1.36 ± 09 m of offset along that profile), which is consistent with a
415 $\overline{\nabla d}$ of 0.54%, that falls into the class of 0.3-1% inferred previously for the distributed
416 deformation mode. Similarly, in the case of profile BB' (Fig. 2b), the unique mode of
417 deformation is the diffuse deformation, and is associated with $\overline{\nabla d}$ of 0.13%, which is within the
418 range of 0.1-0.3% identified as characteristic of the diffuse deformation. Within the range of 0.3-

419 1% that corresponds to the distributed deformation, we additionally distinguish the range 0.3-
420 0.5%, and 0.5-1%, with 0.5% being the theoretical inelastic deformation usually considered (e.g.,
421 Barnhart et al., 2020; Rodriguez Padilla et al., 2022; Scott et al., 2018). Though, in our results,
422 there is no clear difference between the patterns associated with the 0.3-0.5% and the 0.5-1%
423 ranges, and fractures could be observed starting from 0.3%.

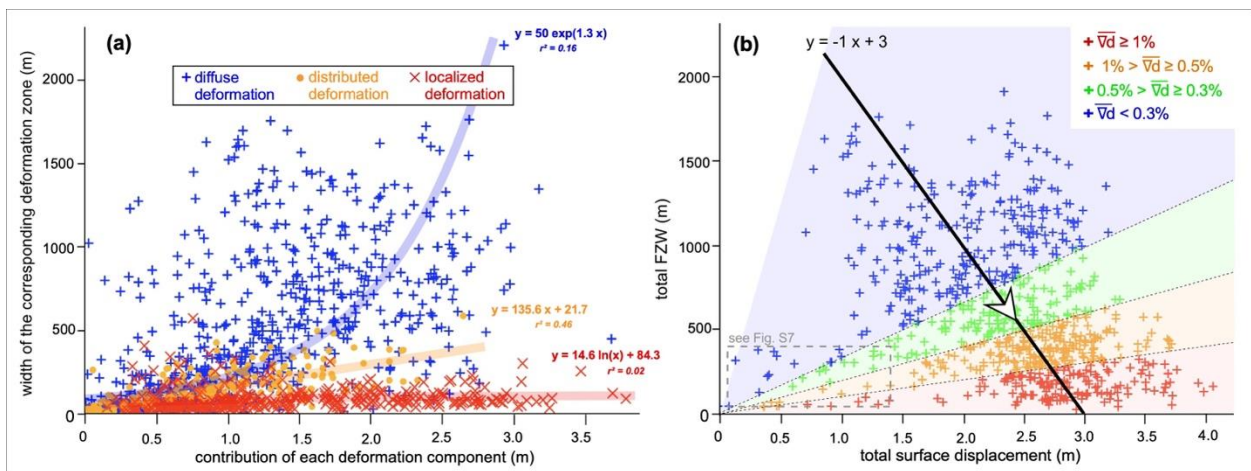
424 Results from the average gradient analysis (Fig. 4b) show that the localized deformation is
425 dominant along most of the primary fault sections, whereas diffuse deformation is dominant
426 along the rupture gaps. This is consistent with our previous surface displacement measurements
427 (Fig. 3a), as well as with the field observations (Figs. 3b and 4b). Hence, $\overline{\nabla d}$ can be used as a
428 parameter to characterize the dominant mode of surface deformation along the 2021 Maduo
429 rupture, along with the more local metric of ∇d that characterizes each deformation mode
430 separately. Each of these different metrics are used hereafter to analyze the behavior of the
431 different deformation components, and to assess possible underlying mechanisms.

432

433 **4.4. Evolution of the width of the localized, distributed, and diffuse deformation zones** 434 **and total FZW**

435 We analyzed the evolution of the width of the localized, distributed, and diffuse deformation
436 zones with respect to their contributions to the surface displacement budget (Figs. 5a and S6).
437 Results show that the width of the diffuse deformation zone increases with increasing amplitude
438 of the diffuse deformation (blue crosses and curve). This increasing trend is best fit (by
439 minimizing the r^2 norm) using an exponential relation, which is coherent with observations from
440 experiments of microcrack development and fracture growth (Chen et al., 2021; Long et al.,
441 2021; J. A. McBeck et al., 2021). The maximum width of the diffuse deformation zone detected

442 for the 2021 Maduo earthquake is ~ 2 km, which also corresponds to the maximum value
 443 obtained for the total FZW. In comparison, the width of the localized deformation zone also
 444 increases with increasing amplitude of the localized deformation (red crosses and curve) but
 445 follows a logarithmic trend, coherent with existing field observations (e.g., Chester et al., 2005;
 446 Mitchell and Faulkner, 2009; Savage and Brodsky, 2011). The width of the localized
 447 deformation region reaches a maximum of about 100 m for any value of localized displacement
 448 about 1.5m or larger. Here, contrasts between the governing equation of FZW with displacement
 449 for the localized and diffuse deformation demonstrates that these two modes of deformation are
 450 controlled by different underlying mechanisms. Finally, the width of the distributed deformation
 451 domain increases linearly with increase distributed deformation, with a maximum detected width
 452 of ~ 500 m (orange crosses and curve). Distributed deformation then appears as a transition
 453 mechanism between the diffuse and localized deformations, consistent with the fact that the
 454 distributed deformation occurs spatially at the transition between the localized and distributed
 455 deformation regions (Figs. 2a and 3a) and is associated with intermediate values of ∇d (Fig. 4).
 456



457
 458 **Figure 5: Scatterplots of evolution of deformation zone width with displacement based on**
 459 **the analysis of the 781 across-fault displacement profiles (Figs. 2c and 3). (a) Evolution, for**

460 each deformation process, of the deformation region for the corresponding displacement
461 amplitude. Similar to **Figure 4a**, each profile is represented by 1 to 3 points. Thick lines
462 propose possible evolution laws for each type of surface deformation. (b) Evolution of the
463 total FZW with increasing total surface displacement. Color code highlights the dominant
464 surface deformation mode, similarly to **Figure 4c**. Black line and white arrow highlight the
465 decrease in total FZW with increasing total surface displacement.

466
467 Considering all the contributions to the surface displacement together, we observe an overall
468 decrease of the total FZW with increasing total surface displacement (black line with white
469 arrow, **Figure 5b**), as previously inferred from the analysis of FZW and displacement
470 measurements along the rupture strike (**Fig. 3a**). Overlapping this result with the average
471 displacement gradient $\overline{\nabla d}$ ranges (color scale, **Fig. 5b**), we observe a decrease in the total FZW
472 that correlates with the increase in $\overline{\nabla d}$, and thus with a greater contribution of the localized
473 deformation on faults with regard to that of the distributed and diffuse deformations. Hence, we
474 propose that two mechanisms are at play here. First, the evolution of the total FZW is controlled
475 by the ratio of the diffuse, on one hand, and localized and distributed, on the other hand,
476 deformation contributions to the total displacement budget (**Fig. 5b**). Second, this ratio decreases
477 with increasing total surface displacement, as a result of greater displacement being
478 accommodated by primary faults (**Fig. 3a**).

479
480 Still, several points corresponding to both the lowest displacement and FZW values (grey dashed
481 box, **Fig. 5b**) remain outside of this decreasing trend, and tend to show a positive relation
482 between total surface displacement and FZW. We suggest this pattern to be characteristic of

483 regions with the smallest displacement values, located at the rupture tips, and experiencing the
484 development of the diffuse deformation zones. This is indeed suggested by geological field
485 observations (Faulkner et al., 2011; Manighetti et al., 2004; Perrin et al., 2016) that describe
486 wider off-fault damage in regions of fault growth. We confirm this inference by separating the
487 points from Figure 5b based on their locations along the rupture strike (Fig. S7). Points that
488 describe this increasing relation are mostly located along the SE rupture tip (blue circle, Fig. S7),
489 which is characterized primarily by surface diffuse deformation (Fig. 3a). The NW tip (green
490 circle, Fig. S7), though, shows a decrease in total FZW with increasing displacement, consistent
491 with the other regions of the rupture. This contrast between the NW and SE rupture tips may
492 reflect different mechanical behaviors between the NW and SE rupture tips due to the contrasts
493 in fault maturity as suggested by Li et al. (2023). Geological field observations indeed show
494 lower accumulated fault displacement along the SE side of the Jiangcuo fault, as a consequence
495 of the eastward long-term fault propagation (Li et al., 2022; Pan et al., 2022), thus in favor of
496 greater diffuse deformation.

497

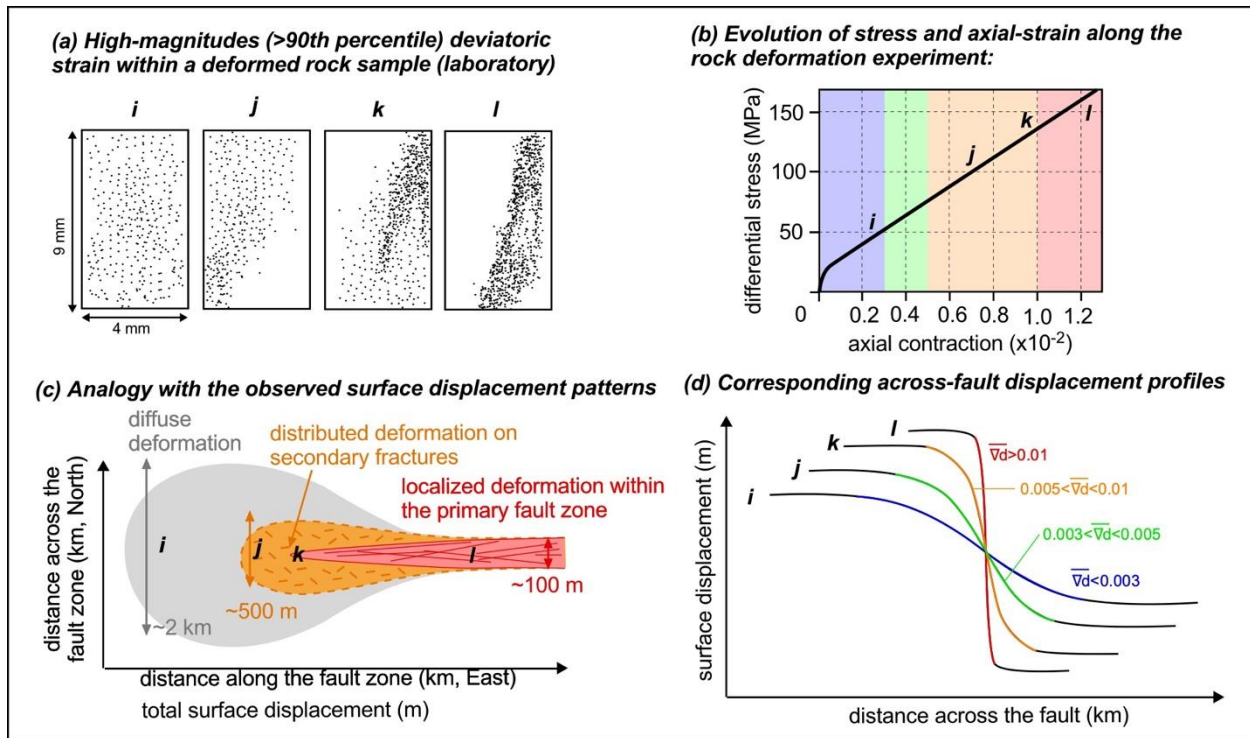
498 **5. Discussion**

499 **5.1. Diffuse inelastic deformation below the rock failure stress: laboratory observations**

500 Diffuse deformation along the 2021 Maduo rupture represents 45.2% of the total surface
501 displacement budget (Fig. 3a), with displacement gradients that range between 0.1 and 0.3%.
502 Such displacement gradient values are below the value of ~0.5% that is usually considered as the
503 minimum strain threshold for the occurrence of surface inelastic deformation (e.g., Barnhart et
504 al., 2020; Cheng and Barnhart, 2021; Li et al., 2023; Milliner, 2021; Scott et al., 2018). However,
505 this value is empirical and primarily based on surface observation of fractures. Laboratory

506 experiments of rock sample deformation in tri-axial compression, though, showed that inelastic
507 deformation actually occurs for lower values of strain, down to ~0.1-0.2%, which is below the
508 actual rock failure stress (e.g., Dong et al., 2023; Lockner, 1998; McBeck et al., 2022, 2021;
509 Thompson et al., 2006; Fig. 6a,b). Such deformation occurs through diffuse microfracturing
510 (phase i, Fig. 6a) for stresses below 75-90% of the failure stress, and before the deformation
511 starts to localize along a defined fault plane (phase j and k, Fig. 6a). This microfracturing is
512 characterized by independent microcracks, homogeneously distributed through the rock sample.
513 Considering that we measure the displacement across the sample, it would bear a similar pattern
514 as the one we observed in the diffuse regions of the Maduo rupture, that is a continuous surface
515 displacement gradient across the FZ. These strong similarities between the deformation patterns
516 described in laboratory experiments and the diffuse deformation patterns observed along the
517 2021 Maduo rupture then strengthen our initial hypothesis which is: surface diffuse deformation
518 along the 2021 Maduo rupture is an inelastic process, and corresponds to diffuse plastic yielding
519 of the off-fault medium below the shallow FZ failure stress.

520



521

522 **Figure 6: Comparison between (a,b) observations of rock deformation from tri-axial**

523 **compression of rock sample in laboratory (mod. from McBeck et al., 2022) and (c,d)**

524 **observations of surface deformation along the 2021 Maduo rupture. (a) View in cross-**

525 **section of the highest-magnitude deviatoric strain values (black points) distribution across**

526 **the rock sample during the experiment, and (b) corresponding stress versus axial-strain**

527 **relation. Color code in (b) highlights the different classes of strain inferred from the $\overline{\nabla d}$**

528 **analysis (see Fig. 4). Letters (i-l) highlight corresponding stages of deformation in (a) and**

529 **(b). (c) Idealized sketch, based on our surface observations along the 2021 Maduo rupture**

530 **(Fig. 3a), of the evolution of the FZ deformation with increasing total surface displacement,**

531 **from (i) a diffuse to (l) a localized deformation mode, through (j,k) a region of mixed**

532 **deformation mode. (d) Surface displacement profiles across the different surface**

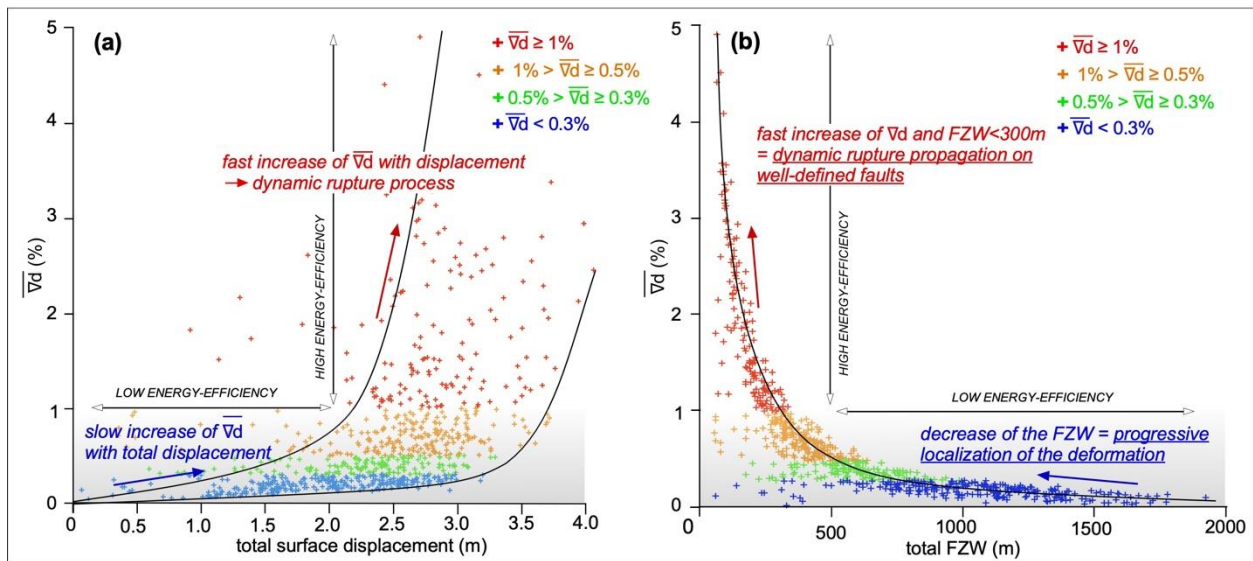
533 **deformation regions (i-l) in (c). In (b,d), color code highlights the different classes of $\overline{\nabla d}$**

534 **(see Fig. 4).**

535

536 Bimodal evolution of $\overline{\nabla d}$ with total displacement (Fig. 7a) and total FZW is also observed (Fig.
537 7b), supporting the co-existence of two different mechanical processes along the 2021 Maduo
538 rupture. On one hand, the diffuse deformation gradient (blue points, Fig. 7) has little sensitivity
539 to variations in the coseismic displacement, highlighting the stable behavior of plastic yielding,
540 but also its low-energy efficiency. Conversely, within the dominantly localized deformation
541 regions (red points, Fig. 7), the displacement gradient has great sensitivity to increases in the
542 displacement gradients, which is consistent with the unstable nature of dynamic fault slip
543 (Collettini et al., 2011; Ikari et al., 2011). Such increase in $\overline{\nabla d}$ in the localized deformation
544 regions do not lead to significant changes in the FZW, showing the ability of the localized
545 deformation to concentrate large amounts of deformation within confined regions, hence
546 representing a highly energy-efficient deformation regime.

547



548

549 **Figure 7: Evolution of the average displacement gradient $\overline{\nabla d}$ with (a) the total surface**
550 **displacement, and (b) the total FZW. Color code highlights the different classes of $\overline{\nabla d}$**

551 including the localized (red), distributed (orange and green), and diffuse (blue)
552 deformations (Fig. 4c). Trends in the data are highlighted with black lines and colored
553 arrows.

554

555 Such comparison between a natural rupture and crystalline rock samples being deformed in the
556 laboratory, is also supported by other deformation experiments in granular porous medium
557 (Aben et al., 2017; Baud et al., 2000; Cilona et al., 2012; Fossen et al., 2007; Visage et al., 2023),
558 as well as field observations (Aubert et al., 2020; Cilona et al., 2012; Micarelli et al., 2006),
559 strengthening our previous interpretations. In the case of the 2021 Maduo rupture, indeed,
560 lithology consists in granular porous carbonate rocks overlaid with unconsolidated quaternary
561 sediments at some locations (Ren et al., 2021; Yuan et al., 2022), which differ from the
562 crystalline nature of the rock used in the experiments described previously. Added to the low-
563 pressure conditions of the shallow crust and interactions with the free-surface, plastic
564 deformation processes can differ from that described previously. In this case, shear and/or
565 dilatation deformation bands (Aben et al., 2017; Aubert et al., 2020; Fossen et al., 2007;
566 Micarelli et al., 2006; Visage et al., 2023), and possibly viscous cataclastic flow (Baud et al.,
567 2000; Cilona et al., 2012) have been suggested as the primarily plastic deformation mechanisms,
568 in addition to the microfracturing occurring in the most consolidated, e.g., cemented and/or
569 healed, regions (Micarelli et al., 2006).

570

571 **5.2. Relations with shallow FZ frictional strength, and the dynamic rupture process**

572 Diffuse deformation along the 2021 Maduo rupture contributes to almost the entire surface
573 displacement budget along the epicentral area, whereas is it a minor component of the surface

574 displacement along the NE and SW rupture sections (Fig. 3a). Based on the previous inference
575 that the diffuse deformation corresponds to plastic yielding below the FZ failure stress (section
576 5.1), it implies that the dynamic stresses due to coseismic rupture in the epicentral area did not
577 overcome the shallow FZ frictional strength. Instead, the stresses associated with the earthquake
578 rupture induced a widespread plastic yielding, which manifests as broad surface diffusive
579 deformation with little surface ruptures.

580

581 Indeed, kinematic slip inversion of the 2021 Maduo event revealed a bilateral pulse-like rupture,
582 with the epicenter area that only slipped during the first 5-8 seconds of the ~40 seconds-long
583 earthquake rupture (Chen et al., 2022; Yuan and Li, 2023; Zheng et al., 2023). Such rupture
584 process resulted in lesser co-seismic displacement in the epicenter area both at depth and at the
585 surface (Hirakawa and Ma, 2016; Wang and Day, 2017), thus showing good correspondence
586 with the patterns we observed at the surface (Fig. 3). The nucleation patch was inferred to be 5~8
587 km wide, and confined within the first 10 km of the crust, supporting the hypothesis of a blind
588 fault rupture and associated surface diffuse deformation. After the first 5-8 seconds, the pulse-
589 like rupture takes over and propagates bilaterally along the fault plane. The propagation is
590 associated with an increase in the slip patch width and amplitude with increasing distance to the
591 epicenter, until it reaches the maximum fault width and ruptures the ground surface. Based on
592 the seismic and geodetic data (e.g., Jin and Fialko, 2021; Liu et al., 2022; Wei et al., 2022; Yuan
593 and Li, 2023; Yue et al., 2022; Zheng et al., 2023; Figs. 1 and 3), and the field observations (Pan
594 et al., 2022; Ren et al., 2022, 2021; Xie et al., 2022; Yuan et al., 2022), the rupture reached the
595 surface at ~30 km on either side of the epicenter. Such rupture process, coupled with shallow FZ

596 frictional strength contrast, would result in smaller shallow coseismic slip and more diffusive
597 deformation in the epicentral area, compared to the NW and SE rupture sections.

598

599 The hypothesis of a stronger shallow FZ frictional strength in the epicenter area is partially
600 supported by the Jiangcuo fault being an immature fault with low slip rate (Pan et al., 2022; Ren
601 et al., 2021) and low accumulated deformation (Li et al., 2022). Locally such frictional strength
602 could also be enhanced by the significant presence of sediments, including quaternary sand-
603 dunes or swampy terrain were observed (Yuan et al., 2022), which typically lead to velocity-
604 strengthening behavior (Ikari et al., 2011; Scholz, 1998). Part of the diffuse deformation also
605 occurred within an area of bedrock (+10 to +25 km SE from the epicenter), but the latter is
606 associated with the highest presence of drainages across the FZ (Yuan et al., 2022), which
607 suggests the presence of recent unconsolidated and wet sediments at the surface. As shown by
608 Hirakawa and Ma (2016), the presence of sediments and/or water could also facilitate the
609 development of a pulse-like rupture, consistent with kinematically constrained rupture process.

610

611 One question about the surface diffuse deformation measured along the epicentral area is
612 whether it relates to the postseismic response of a shallow compliant FZ to a blind fault rupture
613 at depth (Fialko et al., 2002). In this case, one would expect shallow creep to account for this
614 surface elastic deformation. However, shallow afterslip along the 2021 Maduo rupture reaches
615 only ~0.2 m after 1 year (He et al., 2021; Jin and Fialko, 2021; Xiong et al., 2022; Zhao et al.,
616 2021; Zhao et al., 2023). Considering the exponential decrease of afterslip with time, it is thus
617 very unlikely that the shallow layers will account for the 1.5 m of diffuse deformation (Jin et al.,
618 2023). In addition, a majority of this shallow afterslip occur at depth of 2-3 km (Jin et al., 2023),

619 which suggests the surface afterslip is less likely and supports the hypothesis of bulk plastic
620 yielding within the top 1-2 km of the crust. Added to the fact that few sparse fractures were
621 detected at the surface in this region (Figs. 1, and 2b; Liu et al., 2023), showing that inelastic
622 deformation did reach the surface in this area, the diffuse bulk plastic behavior then seems like a
623 reasonable interpretation of the surface diffuse deformation.

624

625 **Conclusions**

626 In this work, we present high-resolution measurements of the surface displacement field along
627 the 2021 $M_w7.4$ Maduo, Tibet, rupture, obtained from the sub-pixel cross-correlation of Pleiades
628 and SPOT6/7 satellite images. These measurements allow for a detailed quantification of the
629 surface displacement along the Maduo fault zone, including the separation of the localized
630 deformation along primary faults, the distributed deformation on secondary fractures, and the
631 bulk diffuse deformation. Results show that diffuse deformation contributed to up to ~45% of the
632 total surface deformation, and generated continuous ground deformation across regions as wide
633 as 2 km. Diffuse deformation is the dominant process within the first 30 km around the
634 earthquake epicenter, whereas other regions of the rupture are primarily characterized by
635 distributed and localized deformations. Our analysis reveals different governing equations for the
636 localized, distributed, and diffuse deformations, suggesting different underlying mechanisms.
637 Comparison with existing laboratory observations of rock deformation, also supported by field
638 and seismic observations, suggest that diffuse deformation corresponds to bulk plastic yielding
639 occurring in regions where the dynamic stresses did not overcome the shallow fault zone
640 frictional strength. Conversely, the localized deformation occurs in regions where the dynamic
641 rupture propagation could be sustained. In the case of the 2021 Maduo rupture, lower dynamic

642 stresses associated with the nascent-pulse-like rupture, combined with greater shallow fault zone
643 strength possibly due to the presence of unconsolidated and/or wet sediments, would favor such
644 shallow diffuse bulk plastic yielding along the epicenter area.

645

646 **Acknowledgments**

647 This work was carried out at the Jet Propulsion Laboratory, California Institute of Technology,
648 under a contract with the National Aeronautics and Space Administration. This work was
649 supported by NASA Decadal Survey Incubator/Surface Topography and Vegetation program,
650 and partly supported by TOSCA CNES and the ANR-18-CE31-0012 projects. This study
651 contributed to the IdEx Université de Paris ANR-18-IDEX-0001. Numerical computations were
652 performed on the GATTACA (JPL, USA), and S-CAPAD/DANTE (IPGP, France) platforms.

653

654 **Open Research**

655 The Pleiades images were provided by the CEOS Seismic Hazards Pilot from ESA
656 (<http://ceos.org/ourwork/workinggroups/disasters/earthquakes>; last accessed on 01/03/24) and
657 the DINAMIS program from CNES (<https://dinamis.teledetection.fr>; <https://cnes.fr>; last
658 accessed on 01/03/24). The SPOT6/7 images were provided by the DINAMIS program and
659 ForM@Ter pole (<https://en.poletterresolide.fr>; last accessed on 01/03/2024) from CNES.
660 Sentinel2 images were accesses at <https://dataspace.copernicus.eu/> (last accessed on 01/03/24).
661 MicMac (<https://github.com/micmacIGN/micmac>; last accessed on 01/03/24) and StackProf
662 (<https://github.com/IPGP/stackprof>; last accessed on 01/03/24) are open source. Supplementary
663 figures providing details on the methodology and on the results of this study are available in the

664 electronic. Surface displacement maps, and fault displacement measurements will be available
665 for the published version of the manuscript.

666

667 **References**

668 Aben, F.M., Doan, M.-L., Gratier, J.-P., Renard, F., 2017. High strain rate deformation of porous
669 sandstone and the asymmetry of earthquake damage in shallow fault zones. *Earth Planet.*
670 *Sci. Lett.* 463, 81–91. <https://doi.org/10.1016/j.epsl.2017.01.016>

671 Ajorlou, N., Hollingsworth, J., Mousavi, Z., Ghods, A., Masoumi, Z., 2021. Characterizing near-
672 field surface deformation in the 1990 Rudbar earthquake (Iran) using optical image
673 correlation. *Geochem. Geophys. Geosystems* 22, 2021 009704.
674 <https://doi.org/10.1029/2021GC009704>

675 Alongi, T., Brodsky, E.E., Kluesner, J., Brothers, D., 2022. Using active source seismology to
676 image the Palos Verdes Fault damage zone as a function of distance, depth, and geology.
677 *Earth Planet. Sci. Lett.* 600, 117871. <https://doi.org/10.1016/j.epsl.2022.117871>

678 Antoine, Klinger, Y., Delorme, A., Wang, K., Bürgmann, R., Gold, R.D., 2021. Diffuse
679 Deformation and Surface Faulting Distribution from Submetric Image Correlation along
680 the 2019 Ridgecrest, California, Ruptures. *Bull. Seismol. Soc. Am.* 111, 2275–2302.
681 <https://doi.org/10.1785/0120210036>

682 Antoine, S.L., Klinger, Y., Delorme, A., Gold, R.D., 2022. Off-Fault Deformation in Regions of
683 Complex Fault Geometries: The 2013, Mw7.7, Baluchistan Rupture (Pakistan). *J.*
684 *Geophys. Res. Solid Earth* 127, e2022JB024480. <https://doi.org/10.1029/2022JB024480>

685 Aubert, I., Léonide, P., Lamarche, J., Salardon, R., 2020. Diagenetic evolution of fault zones in
686 Urgonian microporous carbonates, impact on reservoir properties (Provence – southeast
687 France). *Solid Earth* 11, 1163–1186. <https://doi.org/10.5194/se-11-1163-2020>

688 Barbot, S., Fialko, Y., Sandwell, D., 2008. Effect of a compliant fault zone on the inferred
689 earthquake slip distribution. *J. Geophys. Res. Solid Earth* 113.
690 <https://doi.org/10.1029/2007JB005256>

691 Barnhart, W.D., Gold, R.D., Hollingsworth, J., 2020. Localized fault-zone dilatancy and surface
692 inelasticity of the 2019 Ridgecrest earthquakes. *Nat Geosci* 13, 699–704.
693 <https://doi.org/10.1038/s41561-020-0628-8>

694 Baud, P., Zhu, W., Wong, T., 2000. Failure mode and weakening effect of water on sandstone. *J.*
695 *Geophys. Res. Solid Earth* 105, 16371–16389. <https://doi.org/10.1029/2000JB900087>

696 Budiansky, B., O’connell, R.J., 1976. Elastic moduli of a cracked solid. *Int. J. Solids Struct.* 12,
697 81–97. [https://doi.org/10.1016/0020-7683\(76\)90044-5](https://doi.org/10.1016/0020-7683(76)90044-5)

698 Chen, K., Avouac, J.-P., Geng, J., Liang, C., Zhang, Z., Li, Z., Zhang, S., 2022. The 2021 Mw
699 7.4 Madoi Earthquake: An Archetype Bilateral Slip-Pulse Rupture Arrested at a Splay
700 Fault. *Geophys. Res. Lett.* 49, e2021GL095243. <https://doi.org/10.1029/2021GL095243>

701 Chen, L., Zhang, G., Zou, Z., Guo, Y., Zheng, X., 2021. The effect of fracture growth rate on
702 fracture process zone development in quasi-brittle rock. *Eng. Fract. Mech.* 258, 108086.
703 <https://doi.org/10.1016/j.engfracmech.2021.108086>

704 Cheng, G., Barnhart, W.D., 2021. Permanent Co-Seismic Deformation of the 2013 Mw7.7
705 Baluchistan, Pakistan Earthquake From High-Resolution Surface Strain Analysis. *J.*
706 *Geophys. Res. Solid Earth* 126, 2020 020622. <https://doi.org/10.1029/2020JB020622>

707 Chester, J.S., Chester, F.M., Kronenberg, A.K., 2005. Fracture surface energy of the Punchbowl
708 fault, San Andreas system. *Nature* 437, 133–136. <https://doi.org/10.1038/nature03942>

709 Choi, J., Klinger, Y., Ferry, M., Ritz, J., Kurtz, R., Rizza, M., Bollinger, L., Davaasambuu, B.,
710 Tsend-ayush, N., Demberel, S., 2018. Geologic inheritance and earthquake rupture
711 processes: The 1905 $M \geq 8$ Tsetserleg-Bulnay strike-slip earthquake sequence, Mongolia.
712 *J Geophys Res Solid Earth* 123, 1925–1953. <https://doi.org/10.1002/2017JB013962>

713 Cilona, A., Baud, P., Tondi, E., Agosta, F., Vinciguerra, S., Rustichelli, A., Spiers, C.J., 2012.
714 Deformation bands in porous carbonate grainstones: Field and laboratory observations. *J.*
715 *Struct. Geol., Fault zone structure, mechanics and evolution in nature and experiment* 45,
716 137–157. <https://doi.org/10.1016/j.jsg.2012.04.012>

717 Collettini, C., Niemeijer, A., Viti, C., Smith, S.A.F., Marone, C., 2011. Fault structure, frictional
718 properties and mixed-mode fault slip behavior. *Earth Planet. Sci. Lett.* 311, 316–327.
719 <https://doi.org/10.1016/j.epsl.2011.09.020>

720 Delorme, A., Grandin, R., Klinger, Y., Pierrot-Deseilligny, M., Feuillet, N., Jacques, E., Rupnik,
721 E., Morishita, Y., 2020. Complex Deformation at Shallow Depth During the 30 October
722 2016 Mw6.5 Norcia Earthquake: Interference Between Tectonic and Gravity Processes?
723 *Tectonics* 39, 2019 005596. <https://doi.org/10.1029/2019TC005596>

724 Dong, P., Xia, K., Xu, Y., Elsworth, D., Ampuero, J.-P., 2023. Laboratory earthquakes decipher
725 control and stability of rupture speeds. *Nat. Commun.* 14, 2427.
726 <https://doi.org/10.1038/s41467-023-38137-w>

727 Fan, X., Zhang, G., Zhao, D., Xie, C., Huang, C., Shan, X., 2022. Fault geometry and kinematics
728 of the 2021 Mw 7.3 Maduo earthquake from aftershocks and InSAR observations. *Front.*
729 *Earth Sci.* 10, 993984. <https://doi.org/10.3389/feart.2022.993984>

730 Faulkner, D.R., Mitchell, T.M., Healy, D., Heap, M.J., 2006. Slip on “weak” faults by the
731 rotation of regional stress in the fracture damage zone. *Nature* 444, 922–925.
732 <https://doi.org/10.1038/nature05353>

733 Faulkner, D.R., Mitchell, T.M., Jensen, E., Cembrano, J., 2011. Scaling of fault damage zones
734 with displacement and the implications for fault growth processes. *J. Geophys. Res. Solid*
735 *Earth* 116. <https://doi.org/10.1029/2010JB007788>

736 Fialko, Y., Sandwell, D., Agnew, D., Simons, M., Shearer, P., Minster, B., 2002. Deformation on
737 Nearby Faults Induced by the 1999 Hector Mine Earthquake.
738 <https://doi.org/10.1126/science.1074671>

739 Fialko, Y., Sandwell, D., Simons, M., Rosen, P., 2005. Three-dimensional deformation caused
740 by the Bam, Iran, earthquake and the origin of shallow slip deficit. *Nature* 435, 295–299.
741 <https://doi.org/10.1038/nature03425>

742 Fossen, H., Schultz, R.A., Shipton, Z.K., Mair, K., 2007. Deformation bands in sandstone: a
743 review. *J Geol Soc* 164, 755–769. <https://doi.org/10.1144/0016-76492006-036>

744 Gold, R.D., Reitman, N.G., Briggs, R.W., Barnhart, W.D., Hayes, G.P., Wilson, E., 2015. Onand
745 off-fault deformation associated with the September 2013 Mw 7.7 Balochistan
746 earthquake: Implications for geologic slip rate measurements. *Tectonophysics* 660, 65–
747 78. <https://doi.org/10.1016/j.tecto.2015.08.019>

748 Gombert, B., Duputel, Z., Jolivet, R., Doubre, C., Rivera, L., Simons, M., 2018. Revisiting the
749 1992 Landers earthquake: a Bayesian exploration of co-seismic slip and off-fault damage.
750 *Geophys. J. Int.* 212, 839–852. <https://doi.org/10.1093/gji/ggx455>

751 Ha, G., Liu, J., Ren, Z., Zhu, X., Bao, G., Wu, D., Zhang, Z., 2022. The Interpretation of
752 Seismogenic Fault of the Maduo Mw 7.3 Earthquake, Qinghai Based on Remote Sensing

753 Images—A Branch of the East Kunlun Fault System. *J. Earth Sci.* 33, 857–868.
754 <https://doi.org/10.1007/s12583-021-1556-2>

755 He, K., Wen, Y., Xu, C., Zhao, Y., 2021. Fault Geometry and Slip Distribution of the 2021
756 Mw 7.4 Maduo, China, Earthquake Inferred from InSAR Measurements and Relocated
757 Aftershocks. *Seismol. Res. Lett.* 93, 8–20. <https://doi.org/10.1785/0220210204>

758 He, L., Feng, G., Wu, X., Lu, H., Xu, W., Wang, Y., Liu, J., Hu, J., Li, Z., 2021. Coseismic and
759 Early Postseismic Slip Models of the 2021 Mw 7.4 Maduo Earthquake (Western China)
760 Estimated by Space-Based Geodetic Data. *Geophys. Res. Lett.* 48, e2021GL095860.
761 <https://doi.org/10.1029/2021GL095860>

762 Heap, M.J., Faulkner, D.R., Meredith, P.G., Vinciguerra, S., 2010. Elastic moduli evolution and
763 accompanying stress changes with increasing crack damage: implications for stress
764 changes around fault zones and volcanoes during deformation. *Geophys. J. Int.* 183, 225–
765 236. <https://doi.org/10.1111/j.1365-246X.2010.04726.x>

766 Hearn, E.H., Fialko, Y., 2009. Can compliant fault zones be used to measure absolute stresses in
767 the upper crust? *J. Geophys. Res.* 114, B04403. <https://doi.org/10.1029/2008JB005901>

768 Hirakawa, E., Ma, S., 2016. Dynamic fault weakening and strengthening by gouge compaction
769 and dilatancy in a fluid-saturated fault zone. *J. Geophys. Res. Solid Earth* 121, 5988–
770 6008. <https://doi.org/10.1002/2015JB012509>

771 Ikari, M.J., Marone, C., Saffer, D.M., 2011. On the relation between fault strength and frictional
772 stability. *Geology* 39, 83–86. <https://doi.org/10.1130/G31416.1>

773 Jin, Z., Fialko, Y., 2021. Coseismic and Early Postseismic Deformation Due to the 2021 M7.4
774 Maduo (China) Earthquake. *Geophys. Res. Lett.* 48.
775 <https://doi.org/10.1029/2021GL095213>

776 Jin, Z., Fialko, Y., Yang, H., Li, Y., 2023. Transient Deformation Excited by the 2021 M7.4
777 Maduo (China) Earthquake: Evidence of a Deep Shear Zone. *J. Geophys. Res. Solid*
778 *Earth* 128, e2023JB026643. <https://doi.org/10.1029/2023JB026643>

779 Klinger, Y., Xu, X., Tapponnier, P., Woerd, J., Lasserre, C., King, G., 2005. High-resolution
780 satellite imagery mapping of the surface rupture and slip distribution of the Mw 7.8,
781 Kokoxili earthquake, Kunlun fault, northern Tibet, China.

782 Laws, S., Eberhardt, E., Loew, S., Descoedres, F., 2003. Geomechanical Properties of Shear
783 Zones in the Eastern Aar Massif, Switzerland and their Implication on Tunnelling. *Rock*
784 *Mech. Rock Eng.* 36. <https://doi.org/10.1007/s00603-003-0050-8>

785 Leprince, S., Barbot, S., Ayoub, F., Avouac, J.-P., 2007. Automatic and precise
786 orthorectification, coregistration, and subpixel correlation of satellite images, application
787 to ground deformation measurements. *Geosci Remote Sens IEEE Trans On* 45, 1529–
788 1558. <https://doi.org/10.1109/TGRS.2006.888937>

789 Li, C., Li, T., Hollingsworth, J., Zhang, Y., Qian, L., Shan, X., 2023. Strain Threshold for the
790 Formation of Coseismic Surface Rupture. *Geophys. Res. Lett.* 50, e2023GL103666.
791 <https://doi.org/10.1029/2023GL103666>

792 Li, C., Li, T., Shan, X., Zhang, G., 2022. Extremely Large Off-Fault Deformation during the
793 2021 Mw 7.4 Maduo, Tibetan Plateau, Earthquake. *Seismol. Res. Lett.*
794 <https://doi.org/10.1785/0220220139>

795 Li, Q., Wan, Y., Li, C., Tang, H., Tan, K., Wang, D., 2022. Source Process Featuring
796 Asymmetric Rupture Velocities of the 2021 Mw 7.4 Maduo, China, Earthquake from
797 Teleseismic and Geodetic Data. *Seismol. Res. Lett.* 93, 1429–1439.
798 <https://doi.org/10.1785/0220210300>

799 Liu, J., Hu, J., Li, Z., Ma, Z., Wu, L., Jiang, W., Feng, G., Zhu, J., 2022. Complete three-
800 dimensional coseismic displacements due to the 2021 Maduo earthquake in Qinghai
801 Province, China from Sentinel-1 and ALOS-2 SAR images. *Sci. China Earth Sci.* 65,
802 687–697. <https://doi.org/10.1007/s11430-021-9868-9>

803 Liu, J., Zhijun, L., Liu, X., Milliner, C., Avouac, J.-P., Padilla, A.M.R., Xu, S., Yao, W., Klinger,
804 Y., Han, L., Shao, Y., 2023. Multifault rupture of the 2021
805 *M*_w7.4 Maduo (China) earthquake reveals fault growth toward a
806 stress-favored orientation. Presented at the AGU23, AGU.

807 Liu, X., Chen, Q., Yang, Y., Xu, Q., Zhao, J., Xu, L., Liu, R., 2022. The 2021 Mw7.4 Maduo
808 earthquake: Coseismic slip model, triggering effect of historical earthquakes and
809 implications for adjacent fault rupture potential. *J. Geodyn.* 151, 101920.
810 <https://doi.org/10.1016/j.jog.2022.101920>

811 Lockner, D., 1998. A generalized law for brittle deformation of Westerly granite. *J. Geophys.*
812 *Res.* 103, 5107–5123. <https://doi.org/10.1029/97JB03211>

813 Long, K., Zhang, Z., Ring, U., Faulkner, D., Gamage, R.P., 2021. Microcracks development and
814 porosity evolution in sandstone, Sichuan basin, China: an experimental approach. *Bull.*
815 *Eng. Geol. Environ.* 80, 7717–7729. <https://doi.org/10.1007/s10064-021-02420-1>

816 Lyakhovsky, V., Ben-Zion, Y., 2008. Scaling relations of earthquakes and aseismic deformation
817 in a damage rheology model. *Geophys. J. Int.* 172, 651–662.
818 <https://doi.org/10.1111/j.1365-246X.2007.03652.x>

819 Manighetti, I., King, G., Sammis, C.G., 2004. The role of off-fault damage in the evolution of
820 normal faults. *Earth Planet Sci Lett* 217, 399–408. [https://doi.org/10.1016/S0012-](https://doi.org/10.1016/S0012-821X(03)00601-0)
821 [821X\(03\)00601-0](https://doi.org/10.1016/S0012-821X(03)00601-0)

822 Materna, K., Bürgmann, R., 2016. Contrasts in compliant fault zone properties inferred from
823 geodetic measurements in the San Francisco Bay area. *J. Geophys. Res. Solid Earth* 121,
824 6916–6931. <https://doi.org/10.1002/2016JB013243>

825 McBeck, J., Ben-Zion, Y., Renard, F., 2022. Volumetric and shear strain localization throughout
826 triaxial compression experiments on rocks. *Tectonophysics* 822, 229181.

827 McBeck, J., Ben-Zion, Y., Renard, F., 2021. Fracture Network Localization Preceding
828 Catastrophic Failure in Triaxial Compression Experiments on Rocks. *Front. Earth Sci.* 9.

829 McBeck, J.A., Zhu, W., Renard, F., 2021. The competition between fracture nucleation,
830 propagation, and coalescence in dry and water-saturated crystalline rock. *Solid Earth* 12,
831 375–387. <https://doi.org/10.5194/se-12-375-2021>

832 Micarelli, L., Benedicto, A., Wibberley, C.A.J., 2006. Structural evolution and permeability of
833 normal fault zones in highly porous carbonate rocks. *J. Struct. Geol.* 28, 1214–1227.
834 <https://doi.org/10.1016/j.jsg.2006.03.036>

835 Milliner, C., 2021. Bookshelf Kinematics and the Effect of Dilatation on Fault Zone Inelastic
836 Deformation: Examples From Optical Image Correlation Measurements of the 2019
837 Ridgecrest Earthquake Sequence. *J. Geophys. Res. Solid Earth* 126, 2020 020551.

838 Milliner, C.W.D., 2015. Quantifying near-field and off-fault deformation patterns of the 1992
839 Mw 7.3 Landers earthquake. *Geochem. Geophys. Geosystems* 16, 1577–1598.

840 Milliner, C.W.D., Dolan, J.F., Hollingsworth, J., Leprince, S., Ayoub, F., 2016. Comparison of
841 coseismic near-field and off-fault surface deformation patterns of the 1992 Mw 7.3
842 Landers and 1999 Mw 7.1 Hector Mine earthquakes: Implications for controls on the
843 distribution of surface strain. *Geophys Res Lett* 43, 10,115-10,124.
844 <https://doi.org/10.1002/2016GL069841>

845 Mitchell, T.M., Faulkner, D.R., 2009. The nature and origin of off-fault damage surrounding
846 strike-slip fault zones with a wide range of displacements: A field study from the
847 Atacama fault system, northern Chile. *J. Struct. Geol.* 31, 802–816.
848 <https://doi.org/10.1016/j.jsg.2009.05.002>

849 Nurminen, F., Baize, S., Boncio, P., Blumetti, A.M., Cinti, F.R., Civico, R., Guerrieri, L., 2022.
850 SURE 2.0 – New release of the worldwide database of surface ruptures for fault
851 displacement hazard analyses. *Sci. Data* 9, 729. [https://doi.org/10.1038/s41597-022-](https://doi.org/10.1038/s41597-022-01835-z)
852 [01835-z](https://doi.org/10.1038/s41597-022-01835-z)

853 Okubo, K., 2019. Dynamics, Radiation, and Overall Energy Budget of Earthquake Rupture With
854 Coseismic Off-Fault Damage. *J. Geophys. Res. Solid Earth* 124, 11771–11801.

855 Okubo, K., Bhat, H.S., Rougier, E., Marty, S., Schubnel, A., Lei, Z., Knight, E.E., Klinger, Y.,
856 2019. Dynamics, radiation, and overall energy budget of earthquake rupture with
857 coseismic off-fault damage. *J Geophys Res Solid Earth* 11771–11801.

858 Pan, J., Li, H., Chevalier, M.-L., Tapponnier, P., Bai, M., Li, Chao, Liu, F., Liu, D., Wu, K.,
859 Wang, P., Li, Chunrui, Lu, H., Chen, P., 2022. Co-seismic rupture of the 2021, Mw7.4
860 Maduo earthquake (northern Tibet): Short-cutting of the Kunlun fault big bend. *Earth*
861 *Planet. Sci. Lett.* 594, 117703. <https://doi.org/10.1016/j.epsl.2022.117703>

862 Passelègue, F.X., Pimienta, L., Faulkner, D., Schubnel, A., Fortin, J., Guéguen, Y., 2018.
863 Development and Recovery of Stress-Induced Elastic Anisotropy During Cyclic Loading
864 Experiment on Westerly Granite. *Geophys. Res. Lett.* 45, 8156–8166.
865 <https://doi.org/10.1029/2018GL078434>

866 Perrin, C., Manighetti, I., Ampuero, J.-P., Cappa, F., Gaudemer, Y., 2016. Location of largest
867 earthquake slip and fast rupture controlled by along-strike change in fault structural

868 maturity due to fault growth. *J. Geophys. Res. Solid Earth* 121, 3666–3685.
869 <https://doi.org/10.1002/2015JB012671>

870 Perrin, C., Waldhauser, F., Scholz, C.H., 2021. The Shear Deformation Zone and the Smoothing
871 of Faults With Displacement. *J. Geophys. Res. Solid Earth* 126, e2020JB020447.
872 <https://doi.org/10.1029/2020JB020447>

873 Petersen, M., Dawson, T., Chen, R., Cao, T., Wills, C., Schwartz, D., Frankel, A., 2011. Fault
874 Displacement Hazard for Strike-Slip Faults. *Bull. Seismol. Soc. Am. - BULL Seism.*
875 *SOC AMER* 101, 805–825. <https://doi.org/10.1785/0120100035>

876 Qiu, H., Ben-Zion, Y., Catchings, R., Goldman, M.R., Allam, A.A., Steidl, J., 2021. Seismic
877 Imaging of the Mw 7.1 Ridgecrest Earthquake Rupture Zone From Data Recorded by
878 Dense Linear Arrays. *J. Geophys. Res. Solid Earth* 126, e2021JB022043.
879 <https://doi.org/10.1029/2021JB022043>

880 Ren, J., Xu, X., Zhang, G., Wang, Q., Zhang, Z., Gai, H., Kang, W., 2022. Coseismic surface
881 ruptures, slip distribution, and 3D seismogenic fault for the 2021 Mw 7.3 Maduo
882 earthquake, central Tibetan Plateau, and its tectonic implications. *Tectonophysics* 827,
883 229275. <https://doi.org/10.1016/j.tecto.2022.229275>

884 Ren, J., Zhang, Z., Gai, H., Kang, W., 2021. Typical Riedel shear structures of the coseismic
885 surface rupture zone produced by the 2021 Mw 7.3 Maduo earthquake, Qinghai, China,
886 and the implications for seismic hazards in the block interior. *Nat. Hazards Res.* 1, 145–
887 152. <https://doi.org/10.1016/j.nhres.2021.10.001>

888 Rockwell, T., Lindvall, S., Dawson, T., Langridge, R., Lettis, W., Klinger, Y., 2002. Lateral
889 offsets on surveyed cultural features resulting from the 1999 Izmit and Düzce

890 earthquakes, Turkey. *Bull Seism. Soc Am* 92, 79–94.
891 <https://doi.org/10.1785/0120000809>

892 Rodriguez Padilla, A.M., Oskin, M.E., 2023. Displacement Hazard from Distributed Ruptures in
893 Strike-Slip Earthquakes. *Bull. Seismol. Soc. Am.* <https://doi.org/10.1785/0120230044>

894 Rodriguez Padilla, A.M., Oskin, M.E., Milliner, C.W.D., Plesch, A., 2022. Accrual of
895 widespread rock damage from the 2019 Ridgecrest earthquakes. *Nat. Geosci.* 15, 222–
896 226. <https://doi.org/10.1038/s41561-021-00888-w>

897 Rosu, A.-M., Pierrot-Deseilligny, M., Delorme, A., Binet, R., Klinger, Y., 2015. Measurement of
898 ground displacement from optical satellite image correlation using the free open-source
899 software MicMac. *ISPRS J Photogramm Remote Sens High-Resolut. Earth Imaging*
900 *Geospatial Inf.* 100, 48–59. <https://doi.org/10.1016/j.isprsjprs.2014.03.002>

901 Rupnik, E., Daakir, M., Pierrot Deseilligny, M., 2017. MicMac – a free, open-source solution for
902 photogrammetry. *Open Geospatial Data Softw Stand* 2, 14.
903 <https://doi.org/10.1186/s40965-017-0027-2>

904 Rupnik, E., Deseilligny, M.P., Delorme, A., Klinger, Y., 2016. Refined satellite image
905 orientation in the free open-source photogrammetric tools Apero/MicMac. *ISPRS Ann*
906 *Photogramm Remote Sens* 3, 83–90. <https://doi.org/10.5194/isprsannals-III-1-83-2016>

907 Sammis, C., Rosakis, A., Bhat, H., 2009. Effects of off-fault damage on earthquake rupture
908 propagation: Experimental studies, in: Ben-Zion, Y., Sammis, C. (Eds.), *Mechanics,*
909 *Structure and Evolution of Fault Zones.* Pageoph Topical Volumes, Birkhäuser Basel. pp.
910 1629–1648. https://doi.org/10.1007/978-3-0346-0138-2_5

911 Savage, H.M., Brodsky, E.E., 2011. Collateral damage: Evolution with displacement of fracture
912 distribution and secondary fault strands in fault damage zones. *J. Geophys. Res. Solid*
913 *Earth* 116. <https://doi.org/10.1029/2010JB007665>

914 Scholz, C.H., 1998. Earthquakes and friction laws. *Nature* 391, 37–42.
915 <https://doi.org/10.1038/34097>

916 Scott, C.P., Arrowsmith, J.R., Nissen, E., Lajoie, L., Maruyama, T., Chiba, T., 2018. The M7
917 2016 Kumamoto, Japan, Earthquake: 3-D Deformation Along the Fault and Within the
918 Damage Zone Constrained From Differential Lidar Topography. *J. Geophys. Res. Solid*
919 *Earth* 123, 6138–6155. <https://doi.org/10.1029/2018JB015581>

920 Segall, P., 2010. *Earthquake and Volcano Deformation*, STU-Student. ed. Princeton University
921 Press.

922 Simone, B., Andrenacci, C., Daniele, C., Scott, C., Brozzetti, F., Arrowsmith, R., Lavecchia, G.,
923 2022. High-Detail Fault Segmentation: Deep Insight into the Anatomy of the 1983 Borah
924 Peak Earthquake Rupture Zone (Mw 6.9, Idaho, USA). *Lithosphere* 2022.
925 <https://doi.org/10.2113/2022/8100224>

926 Teran, O.J., 2015. Geologic and structural controls on rupture zone fabric: A field-based study of
927 the 2010 Mw 7.2 El Mayor–Cucapah earthquake surface rupture. *Geosphere* 11, 899–
928 920.

929 Thomas, M.Y., Bhat, H.S., 2018. Dynamic evolution of off-fault medium during an earthquake:
930 a micromechanics based model. *Geophys. J. Int.* 214, 1267–1280.
931 <https://doi.org/10.1093/gji/ggy129>

932 Thompson, B.D., Young, R.P., Lockner, D.A., 2006. Fracture in Westerly Granite under AE
933 Feedback and Constant Strain Rate Loading: Nucleation, Quasi-static Propagation, and

934 the Transition to Unstable Fracture Propagation. *Pure Appl. Geophys.* 163, 995–1019.
935 <https://doi.org/10.1007/s00024-006-0054-x>

936 Torabi, A., Johannessen, M., Ellingsen, T., 2019. Fault Core Thickness: Insights from
937 Siliciclastic and Carbonate Rocks. *Geofluids* 2019, 1–24.
938 <https://doi.org/10.1155/2019/2918673>

939 Vidale, J.E., Li, Y.-G., 2003. Damage to the shallow Landers fault from the nearby Hector Mine
940 earthquake. *Nature* 421, 524–526. <https://doi.org/10.1038/nature01354>

941 Visage, S., Souloumiac, P., Cubas, N., Maillot, B., Antoine, S.L., Delorme, A., Klinger, Y.,
942 2023. Evolution of the off-fault deformation of strike-slip faults in a sand-box
943 experiment. *Tectonophysics* 847, 229704. <https://doi.org/10.1016/j.tecto.2023.229704>

944 Wang, W., Fang, L., Wu, J., Tu, H., Chen, L., Lai, G., Zhang, L., 2021. Aftershock sequence
945 relocation of the 2021 MS7.4 Maduo Earthquake, Qinghai, China. *Sci. China Earth Sci.*
946 64, 1371–1380. <https://doi.org/10.1007/s11430-021-9803-3>

947 Wang, Y., Day, S.M., 2017. Seismic source spectral properties of crack-like and pulse-like
948 modes of dynamic rupture. *J. Geophys. Res. Solid Earth* 122, 6657–6684.
949 <https://doi.org/10.1002/2017JB014454>

950 Wei, S., Zeng, H., Shi, Q., Liu, J., Luo, H., Hu, W., Li, Y., Wang, W., Ma, Z., Liu-Zeng, J.,
951 Wang, T., 2022. Simultaneous Rupture Propagation Through Fault Bifurcation of the
952 2021 Mw7.4 Maduo Earthquake. *Geophys. Res. Lett.* 49, e2022GL100283.
953 <https://doi.org/10.1029/2022GL100283>

954 Xie, H., Li, Z., Yuan, D., Wang, X., Su, Q., Li, X., Wang, A., Su, P., 2022. Characteristics of
955 Co-Seismic Surface Rupture of the 2021 Maduo Mw 7.4 Earthquake and Its Tectonic

956 Implications for Northern Qinghai–Tibet Plateau. *Remote Sens.* 14, 4154.
957 <https://doi.org/10.3390/rs14174154>

958 Xiong, W., Chen, W., Wang, D., Wen, Y., Nie, Z., Gang, L., Dijin, W., Yu, P., Qiao, X., Zhao,
959 B., 2022. Coseismic slip and early afterslip of the 2021 Mw 7.4 Maduo, China
960 earthquake constrained by GPS and InSAR data. *Tectonophysics* 840, 229558.
961 <https://doi.org/10.1016/j.tecto.2022.229558>

962 Yamamoto, K., Sato, N., Yabe, Y., 2002. Elastic property of damaged zone inferred from in-situ
963 stresses and its role on the shear strength of faults. *Earth Planets Space* 54, 1181–1194.
964 <https://doi.org/10.1186/BF03353319>

965 Yang, H., 2015. Recent advances in imaging crustal fault zones: a review. *Earthq. Sci.* 28, 151–
966 162. <https://doi.org/10.1007/s11589-015-0114-3>

967 Yang, H., Zhu, L., Cochran, E.S., 2011. Seismic structures of the Calico fault zone inferred from
968 local earthquake travel time modelling. *Geophys. J. Int.* 186, 760–770.
969 <https://doi.org/10.1111/j.1365-246X.2011.05055.x>

970 Yang, Y.-H., Xu, Q., Hu, J.-C., Wang, Y.-S., Dong, X.-J., Chen, Q., Zhang, Y.-J., Li, H.-L.,
971 2022. Source Model and Triggered Aseismic Faulting of the 2021 Mw 7.3 Maduo
972 Earthquake Revealed by the UAV-Lidar/Photogrammetry, InSAR, and Field
973 Investigation. *Remote Sens.* 14, 5859. <https://doi.org/10.3390/rs14225859>

974 Yuan, J., Li, Y., 2023. Complex fault geometry controls dynamic rupture of the 2021 Mw7.4
975 Maduo earthquake, NE Tibetan Plateau. *Tectonophysics* 230105.
976 <https://doi.org/10.1016/j.tecto.2023.230105>

977 Yuan, Z., Li, T., Su, P., Sun, H., Ha, G., Guo, P., Chen, G., Jobe, J., 2022. Large Surface-
978 Rupture Gaps and Low Surface Fault Slip of the 2021 Mw 7.4 Maduo Earthquake Along

979 a Low-Activity Strike-Slip Fault, Tibetan Plateau. *Geophys. Res. Lett.* 49.
980 <https://doi.org/10.1029/2021GL096874>

981 Yuan, Z., Liu-Zeng, J., Li, X., Xu, J., Yao, W., Han, L., Li, T., 2020. Detailed mapping of the
982 surface rupture of the 12 February 2014 Yutian Ms7.3 earthquake, Altyn Tagh fault,
983 Xinjiang, China. *Sci. China Earth Sci.* 64. <https://doi.org/10.1007/s11430-020-9673-6>

984 Yue, H., Shen, Z.-K., Zhao, Z., Wang, T., Cao, B., Li, Z., Bao, X., Zhao, L., Song, X., Ge, Z.,
985 Ren, C., Lu, W., Zhang, Y., Liu-Zeng, J., Wang, M., Huang, Q., Zhou, S., Xue, L., 2022.
986 Rupture process of the 2021 M7.4 Maduo earthquake and implication for deformation
987 mode of the Songpan-Ganzi terrane in Tibetan Plateau. *Proc. Natl. Acad. Sci.* 119,
988 e2116445119. <https://doi.org/10.1073/pnas.2116445119>

989 Zhang, X., Feng, W., Du, H., Samsonov, S., Yi, L., 2022. Supershear Rupture During the 2021
990 MW 7.4 Maduo, China, Earthquake. *Geophys. Res. Lett.* 49, e2022GL097984.
991 <https://doi.org/10.1029/2022GL097984>

992 Zhao, D., Qu, C., Bürgmann, R., Shan, X., 2023. Characterizing Deep, Shallow, and Surface
993 Fault Zone Deformation of the 2021 Mw 7.4 Maduo, China, Earthquake. *Seismol. Res.*
994 *Lett.* <https://doi.org/10.1785/0220230115>

995 Zhao, D., Qu, C., Chen, H., Shan, X., Song, X., Gong, W., 2021. Tectonic and Geometric
996 Control on Fault Kinematics of the 2021 Mw7.3 Maduo (China) Earthquake Inferred
997 From Interseismic, Coseismic, and Postseismic InSAR Observations. *Geophys. Res. Lett.*
998 48. <https://doi.org/10.1029/2021GL095417>

999 Zhao, L., Xu, W., Xie, L., Zhao, D., Zhu, Z., Wu, P., Guo, H., 2023. Fault geometry and low
1000 frictional control of the near-field postseismic deformation of the 2021 Mw 7.3 Maduo
1001 earthquake. *Tectonophysics* 863, 230000. <https://doi.org/10.1016/j.tecto.2023.230000>

1002 Zheng, A., Yu, X., Qian, J., Liu, X., Zhang, W., Chen, X., Xu, W., 2023. Cascading rupture
1003 process of the 2021 Maduo, China earthquake revealed by the joint inversion of seismic
1004 and geodetic data. *Tectonophysics* 849, 229732.
1005 <https://doi.org/10.1016/j.tecto.2023.229732>

1006 Zhou, Z., Bianco, M., Gerstoft, P., Olsen, K., 2022. High-Resolution Imaging of Complex
1007 Shallow Fault Zones Along the July 2019 Ridgecrest Ruptures. *Geophys. Res. Lett.* 49,
1008 e2021GL095024. <https://doi.org/10.1029/2021GL095024>

1009